

# Universal behaviour in boundary-driven electrokinetic flows

Ahis Shrestha<sup>1,2</sup> , Eleftherios Kirkinis<sup>1,3</sup> and Monica Olvera de la Cruz<sup>1,2,3</sup>

<sup>1</sup>Center for Computation and Theory of Soft Materials, Northwestern University, Evanston, IL 60208, USA

<sup>2</sup>Department of Physics and Astronomy, Northwestern University, Evanston, IL 60208, USA

<sup>3</sup>Department of Materials Science & Engineering, Robert R. McCormick School of Engineering and Applied Science, Northwestern University, Evanston, IL 60208, USA

**Corresponding author:** Eleftherios Kirkinis, [kirkinis@northwestern.edu](mailto:kirkinis@northwestern.edu)

(Received 27 January 2024; revised 28 February 2025; accepted 12 March 2025)

Travelling wave charges lying on the insulating walls of an electrolyte-filled capillary give rise to oscillatory modes which vanish when averaged over the period of oscillation. They also give rise to a zero mode (a unidirectional, time-independent velocity component) which does not vanish. The latter is a nonlinear effect caused by continuous symmetry breaking due to the quadratic nonlinearity associated with the electric body force in the time-dependent Stokes equations. In this paper, we provide a unified view of the effects arising in boundary-driven electrokinetic flows (travelling wave electroosmosis) and establish the universal behaviour exhibited by the observables. We show that the incipient velocity profiles are self-similar implying that those obtained with a single experimental configuration can be employed again to attain further insights without the need of repeating the experiment. Certain results from the literature are recovered as special cases of our formulation and we resolve certain paradoxes having appeared in the past. We present simple theoretical expressions, depending on a single-fit parameter, that reproduce these profiles, which could thus provide a rapid test of consistency between our theory and future experiment. The effect becomes more pronounced when reducing the transverse dimension of the system, relative to the velocity direction, and increasing the excitation wavelength, and can therefore be employed for unidirectional transport of electrolytes in thin and long capillaries. General relations, expressing the zero mode velocity in terms of the electric potential and the geometry of the system only, can thus be easily adapted to alternative experimental settings.

**Key words:** electrokinetic flows, coupled diffusion and flow

## 1. Introduction

Microfluidic devices can be classified according to their degree of configurability (Paratore *et al.* 2022, Box 2). In the static state, the geometry of the device is set once and for all at the manufacturing level. In the configurable state, the user can format the device only to specific predefined states. Additionally, in the reconfigurable state, the device can be rearranged at will in real time. As discussed by Paratore *et al.* (2022), travelling wave electroosmosis can be considered to belong to the third class (reconfigurable) by shaping complex flow patterns using a suitable array of electrodes. Among its applications, this concept can be employed as a diagnostic personalised tool employing very low voltages (1.5 V, as was also predicted by Cahill *et al.* (2004)) and tunable frequencies, with low power consumption and cost-effective manufacturing based on recent metal-oxide-semiconductor technologies (Yen *et al.* 2019).

Travelling wave electroosmosis is a special, boundary-guided electrokinetic effect whereby a body force is exerted on the bulk charges of an electrolyte due to a travelling wave charge or voltage excitation on the capillary walls. Since the liquid is viscous, it is being dragged along with the charges, thus providing control over its movement. Electrolyte pumping with travelling wave wall charges was introduced in the seminal, but largely overlooked, work of Ehrlich & Melcher (1982) who showed numerically that an electrolyte separated by an electrode array with a thick dielectric layer will move unidirectionally parallel to the charged wall – a velocity profile that will be termed zero mode in the present paper. Cahill *et al.* (2004), Ramos *et al.* (2005) and García-Sánchez *et al.* (2006) established the existence of this unidirectional flow in travelling wave electroosmosis experimentally and proposed some theoretical models. Note that AC electroosmosis is a related effect whereby AC signals in the kHz range are employed to generate regions of circulating liquid flow, periodically changing their sense of circulation (González *et al.* 2000; Green *et al.* 2000). Invoking a geometrical asymmetry, one can also generate unidirectional flow (cf. Ajdari 2000).

Most theoretical and numerical electroosmosis works with non-uniformly charged walls employ Neumann boundary conditions, that is, the normal component of the electric field to a wall is fixed by the commensurate charge distribution, see for instance Ajdari (1995) and Kamsma *et al.* (2023a,b). However, most experimental works and their accompanying theories employed Dirichlet boundary conditions, that is, they fix the electric potential on the walls (e.g. Cahill *et al.* 2004; González *et al.* 2008). In the literature, there is no established argument to justify the use of one or the other. They lead to different predictions and it is not apparent if there is any relationship between them. A fundamental physical justification for the presence of the unidirectionally observed flow (termed the zero mode here) is still lacking. There is no scaling argument in the literature that would classify the observed flows in a universal manner. The approximations involved usually require small frequencies,  $\omega \ll Dk\kappa$ , where  $\kappa$  is the inverse Debye length and  $k$  is the excitation wavenumber to be defined below (cf. Ramos *et al.* 2005; González *et al.* 2008). It is common practice in the literature to separate the spatial domain into several adjacent regions over which different equations apply. This also requires the introduction of different material parameters in each region not necessarily known *a priori*. The current state-of-the-art is based on different configurations, boundary conditions, liquids etc., making it hard, if not impossible, to reach a unified view of the observed effects. In addition, velocity profiles that appeared in the published literature (Ehrlich & Melcher 1982) are not associated with a vector quantity which, upon reversal, would also reverse the direction of the (zero mode) velocity, creating an ambiguity on the nature of the

mechanism that drives the flow. We will address all these issues in turn and we will unveil the universal aspects of the flow, as described below.

In this paper, we develop a hydrodynamic theory for the unidirectional motion of an electrolyte when the bounding walls (of a semi-infinite space, channel or cylindrical capillary) are insulating and carry a travelling wave charge distribution  $\sigma = \sigma_0 e^{i(\mathbf{k} \cdot \mathbf{x} - \omega t)}$  (Neumann boundary conditions for the Poisson equation), where  $\mathbf{k}$  and  $\omega$  are the wavevector and angular frequency, respectively, of the plane wave. After averaging over the period of oscillations, we show that the non-vanishing electrolyte velocity profiles (that we term the zero-mode) are self-similar and only depend on three groups of dimensionless parameters. With this realisation, it is possible to draw conclusions for the system behaviour based on different liquids, charge distributions, electric field amplitudes, frequencies etc. by just performing a single experiment. We repeat the above development for the case of Dirichlet boundary conditions for the Poisson equation (travelling wave electric potential  $\phi = \phi_0 e^{i(\mathbf{k} \cdot \mathbf{x} - \omega t)}$  at the wall) and show that self-similar profiles also exist but for different dimensionless groups. In particular, while the Neumann problem requires that the excitation frequency  $\omega$  is normalised by the Debye time scale  $\tau_D$ , where  $\tau_D^{-1} = D\kappa^2$ , the Dirichlet problem frequency, is normalised by  $\tau_{k\kappa}^{-1} = Dk\kappa$  (semi-infinite space) and by  $\tau_k^{-1} = Dk^2$  (channel case). Thus, Neumann boundary conditions seem to furnish a more robust and consistent behaviour, relative to their Dirichlet counterparts, at all configurations since its dimensionless group does not depend on geometry. We note that this predominance of Neumann versus their Dirichlet counterparts has already been pointed out in the literature of electrokinetic energy conversion and its efficiency in nanofluidic channels by matching theory (van der Heyden *et al.* 2006) with experiment (van der Heyden *et al.* 2007). In addition, variational formulations employ the Neumann conditions as natural boundary conditions in general and in the solution of the Poisson–Boltzmann equation in particular (Clarke & Stiles 2015). We perform finite-element numerical simulations of the full equations (with the Neumann boundary conditions) and find good agreement with their exact counterparts in an order-of-magnitude basis and in their general trend. A well-known principle, called Stokes’ rule (Zauderer 1989, p. 258) then explains the relationship between the Neumann and the Dirichlet results (cf. Appendix G).

We introduce simple theoretical expressions (theory fits) that reproduce the self-similar profiles and only depend on a single-fit parameter  $\beta$ , which could thus provide a rapid test of consistency between our theory and future experiment. We show that our order-of-magnitude estimates of the liquid velocity derived with the Neumann theory might agree well with experiment. This is to be contrasted with theories, directly or indirectly based on Dirichlet conditions, which provide much higher estimates in comparison to the measurements of their accompanying experiments (cf. Cahill *et al.* 2004; Ramos *et al.* 2005).

We show that the fluid velocity with Neumann conditions becomes prominent by decreasing the transverse size of the device, relative to the direction of the velocity, or by increasing the excitation wavelength, and thus could be used for unidirectional electrolyte transport in thin and long devices. This behaviour was numerically established before (cf. figure 6f of Liu *et al.* (2018)).

The travelling wave wall charge-induced unidirectional velocity is a zero or massless or soft or Goldstone mode (Goldstone 1961). The existence of a zero mode is associated with broken continuous symmetries (Negele & Orland 1988) and its presence here is not surprising as it is well known that it arises in problems involving quadratic nonlinearities, such as the Kuramoto–Sivashinskii equation (cf. Malomed 1992;

Kirkinis & O'Malley Jr. 2014). Here, the quadratic nonlinearity is due to the electric body force in the momentum equation.

Certain results from the literature are recovered as special cases of our formulation (for instance, we recover the Ramos *et al.* (2005) theoretical expression for the unidirectional velocity) and we resolve certain paradoxes that appeared before (for instance, that the travelling wave electroosmosis solution of Ehrlich & Melcher (1982) is singular). We derive general formulae, for the 'slip' or average velocities that only depend on the form taken by the electric potential and the geometry of the system. This is useful since these formulae can be adopted 'as is' even when different boundary conditions of the electric problem are employed.

In this paper, we invoke the Debye–Falkenhagen approximation (Bazant, Thornton & Ajdari 2004), a necessary step towards retaining the time-dependence of the Nernst–Planck equation. We are unaware of any study of its range of validity; we thus provide such a detailed analysis, which can only be carried out on an *a posteriori* basis. We show that the approximation is superior to its Debye–Hückel counterpart and its validity increases with increasing excitation frequency  $\omega$ . To avoid any confusion, we emphasise that the term 'nonlinear', employed in this paper, refers to the form of the governing partial differential equations endowed with a quadratic nonlinearity in the momentum equation and is not associated with retaining the Boltzmann form of the species concentrations.

This paper is organised as follows. Section 2 introduces the governing equations and boundary conditions of a nonlinear formulation of the electroosmosis problem when the electrolyte is driven by travelling wave charge distributions on the channel walls (or driven by travelling wave wall electric potentials). In § 3, we consider the electrolyte filling the semi-infinite space  $z > 0$ , driven by a travelling wave charge distribution at the wall  $z = 0$  with wavenumber  $k$ . We show that the zero mode velocity at  $z = \infty$  (customarily referred to in the literature as the 'slip velocity') is self-similar with respect to three dimensionless groups and that a simple expression can be employed to describe these profiles. In § 3.2, we provide estimates of the velocity magnitude for standard experimental parameters and show that they agree well, in order-of-magnitude, with existing measurements, in contrast to their Dirichlet theoretical counterparts.

In § 4, we consider travelling charge distributions on both walls of a channel giving rise to a zero mode (that is, unidirectional and time-independent) velocity field. This configuration choice is dictated by results showing that the ideal and optimal geometry requires in-phase and symmetrical electrode arrays with respect to the channel centre (Yeh, Yang & Luo 2011). The zero mode velocity averaged over the channel width is again self-similar and is compared with its (also self-similar) Dirichlet counterpart. The flow velocity increases by reducing the channel size, reaching a steady value. In § 5, we reconsider the nonlinear electroosmosis problem but now in a cylindrical capillary whose wall carries travelling wave charges. We reach similar conclusions to the channel case regarding the presence of the zero mode and its various limits.

In § 6, we employ numerical simulations of the Poisson–Nernst–Planck–Navier–Stokes system (in the low-Péclet-number approximation) to obtain the zero mode velocity and compare it with its exact counterparts developed in the previous sections. Details of the numerical scheme employed are delegated to a supplementary materials addendum. Therein, we briefly discuss the effect a finite Péclet number has on the velocity magnitude.

We conclude this paper with a number of Appendices. These include an analysis of the validity of the Debye–Falkenhagen approximation, the solution of the Poisson–Nernst–Planck problem for Dirichlet boundary conditions and a discussion of the  $k$ -dependence of the various velocities derived in the main body of this article. We show that if the zero-mode velocity is taken into account in the Nernst–Planck equation, the observables

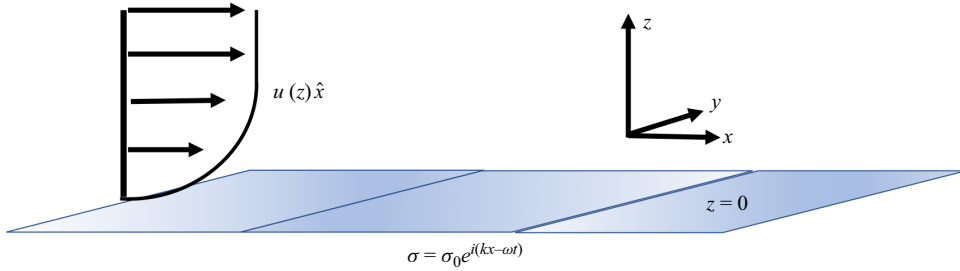


Figure 1. Wall travelling wave charges give rise to a nonlinear body force and torque (see (2.8)) in a 1 : 1 electrolyte lying in the semi-infinite space  $z > 0$ , leading to the appearance of a unidirectional fluid velocity in the  $\hat{x}$  direction, parallel to the wall, that is quadratic with respect to the associated electric field and that does not vanish after averaging over the charge period of oscillation.

are not significantly affected for moderate values of the Péclet number, cf. [Appendix B.2](#). In [Appendix C](#), we show that the travelling wave electroosmosis solution of Ehrlich & Melcher (1982) is singular and that the commensurate zero mode velocity field is non-unique.

## 2. Governing equations of travelling wave electroosmosis

Consider the application of travelling wave charges

$$\sigma(x, t) = \sigma_0 e^{i(kx - \omega t)} \quad (2.1)$$

on an insulating wall, temporarily identified with the plane  $z = 0$ , cf. [figure 1](#), with real frequency  $\omega$  and real wave vector  $\mathbf{k} = k\hat{x}$ . We consider a 1 : 1 electrolyte where each concentration species is  $c_{\pm} = c_{\infty} + \delta c_{\pm}$  containing a perturbation  $\delta c_{\pm}$  superposed on its uniform counterpart  $c_{\infty}$ . Thus, the bulk charge distribution is  $\rho = e(\delta c_{+} - \delta c_{-})$  while the salt distribution is  $s \sim 2ec_{\infty}$ , to leading order, where  $e$  is the proton charge. This implies that  $s$  is also accompanied by a perturbation  $e(\delta c_{+} + \delta c_{-})$ , which however is never invoked in this paper but it can be computed, need be. The validity of this approximation can only be examined *a posteriori* and in conjunction to the reductive form of the Nernst–Planck equation, as detailed below. We carry-out such an analysis in [Appendix A.1](#).

Invoking the aforementioned approximation and the Poisson equation for the electric potential  $\phi$ ,

$$\nabla^2 \phi = -\frac{\rho}{\epsilon}, \quad (2.2)$$

where  $\epsilon$  is the dielectric constant, the evolution of charge distribution,

$$\partial_t \rho = D \left[ \nabla^2 \rho + \frac{e}{k_B T} \nabla \cdot (s \nabla \phi) \right] - \mathbf{v} \cdot \nabla \rho, \quad (2.3)$$

reduces to the Debye–Falkenhagen equation (Bazant *et al.* 2004)

$$\partial_t \rho = D \left[ \nabla^2 \rho - \kappa^2 \rho \right] - \partial_x \rho \partial_z \psi + \partial_z \rho \partial_x \psi. \quad (2.4)$$

Here,  $\mathbf{v}$  is the electrolyte velocity,  $D$  is the charge diffusion coefficient (assumed to have the same value for both species),  $k_B T$  the thermal energy and  $\psi = \psi(x, z, t)$  is the streamfunction for a two-dimensional incompressible liquid, whereby

$$\mathbf{v} = (u, 0, w) = \left( \frac{\partial \psi}{\partial z}, 0, -\frac{\partial \psi}{\partial x} \right), \quad (2.5)$$

and

$$\kappa = \left[ \frac{2e^2 c_\infty}{\epsilon k_B T} \right]^{\frac{1}{2}} \quad (2.6)$$

is the inverse Debye length. How this approximation relates to its classical Debye–Hückel counterpart (where  $\rho = -\epsilon\kappa^2\phi$  everywhere) is discussed in [Appendix A.2](#).

Even in the absence of the last two (nonlinear advective) terms, (2.4) leads to a non-equilibrium charge distribution  $\rho$ , where the charge changes both in time and in space, in contrast to the essentially equilibrium route taken in the literature (cf. Probst [1994](#)). Equation (2.4) is not new and has been derived earlier, for instance, by Cahill *et al.* ([2004](#)) and Mortensen *et al.* ([2005](#)) following the older results of Ehrlich & Melcher ([1982](#)).

In the main body of this paper, we will adopt the low-Péclet-number limit, thus reducing (2.4) to

$$\partial_t \rho = D \left[ \nabla^2 \rho - \kappa^2 \rho \right]. \quad (2.7)$$

We justify the small-Péclet-number approximation in [Appendix B.1](#). We show in [Appendix B.2](#) that retaining the advection terms in (2.4), based on the zero velocity mode only, does not lead to a significant change in the observables for moderate values of the Péclet number.

Finally, the streamfunction  $\psi$  satisfies

$$\rho_l \partial_t \nabla^2 \psi = \eta \nabla^4 \psi + \partial_x \rho \partial_z \phi - \partial_z \rho \partial_x \phi, \quad (2.8)$$

where  $\rho_l$  is the liquid electrolyte mass density and  $\psi(x, 0, t) = 0 = \partial_z \psi(x, 0, t)$  (the no-slip boundary condition) assuming temporarily that the solid boundary is identified with the plane  $z = 0$ . If the flow extends to infinity, then its velocity is considered to have a finite value there.

All results of the present section depend on the (weakly) nonlinear character of the nonlinear torque (last two terms) in (2.8). Although, in general, the commensurate velocity field vanishes when averaged over the period of oscillation of the applied electric field, there are circumstances where this is not so. This is due to the presence of a zero mode that arises due to constructive interference of the charge and potential excitations arising in (2.8). The nonlinear effect described in (2.8) vanishes if the charge and the potential do not vary in the direction parallel to the wall (the  $x$ -direction). Likewise, in the  $\omega \equiv 0$  case, the nonlinear torque in (2.8) vanishes, on account of the connection  $\rho = -\epsilon\kappa^2\phi$  (the Debye–Hückel approximation), or equivalently, the electric body force is the gradient of a scalar field and thus only affects the pressure distribution.

## 2.1. Boundary conditions

In this paper, we will predominantly consider Neumann boundary conditions for the Poisson equation (2.2), at a solid wall carrying a surface charge  $\sigma$  as in (2.1), where

$$\hat{\mathbf{n}} \cdot \nabla \phi = -\frac{\sigma}{\epsilon}, \quad \text{at a charged wall}, \quad (2.9)$$

with the unit normal vector  $\hat{\mathbf{n}}$  pointing into the liquid. We will consider also the case where the current of bulk charge  $\rho$  vanishes at wall, that is,

$$\mathbf{J} \cdot \hat{\mathbf{n}} \equiv -D \left[ \nabla \rho + \frac{e}{k_B T} s \nabla \phi \right] \cdot \hat{\mathbf{n}} = 0, \quad \text{at a charged wall}. \quad (2.10)$$



Quantity	Value	Definition
$\omega$ (rad · s <sup>-1</sup> )	Arbitrary	Wall travelling wave charge frequency
$\Delta = \sqrt{2D/\omega}$ (cm)		Charge penetration depth (cf. (3.3))
$k$ (m <sup>-1</sup> )	10 <sup>1</sup> –10 <sup>5</sup>	Wall charge wavenumber
$\kappa$ (m <sup>-1</sup> )	10 <sup>2</sup> –10 <sup>8</sup>	Inverse Debye length
$K = \sqrt{k^2 + \kappa^2}$ (m <sup>-1</sup> )		
$p = ((1+i)/\Delta)$ (m <sup>-1</sup> )		Charge oscillating complex wavenumber (cf. (3.3))
$P = \sqrt{p^2 - k^2 - \kappa^2}$ (m <sup>-1</sup> )		Charge complex wavenumber (cf. (3.3))
$\eta$ (kg m <sup>-1</sup> s <sup>-1</sup> )	10 <sup>-3</sup>	Electrolyte dynamic viscosity
$\nu$ (m <sup>2</sup> s <sup>-1</sup> )	10 <sup>-5</sup>	Electrolyte kinematic viscosity
$2h$ (m)	10 <sup>-2</sup> –10 <sup>-5</sup>	Channel width
$a$ (m)	10 <sup>-2</sup> –10 <sup>-5</sup>	Capillary radius
$u$ (m s <sup>-1</sup> )	10 <sup>-4</sup>	Horizontal (zero mode) velocity component
$u_0, u_1$ (m s <sup>-1</sup> )		Horizontal velocity scales, cf. Eq. (2.12)
$D$ (m <sup>2</sup> s <sup>-1</sup> )	10 <sup>-9</sup>	Diffusion coefficient for electrolyte charges
$\sigma, \sigma_0$ (C m <sup>-2</sup> )		Wall charge distribution
$E \equiv \sigma_0/\epsilon$ (V m <sup>-1</sup> )	10 <sup>5</sup>	Electric field induced by $\sigma$
$\epsilon$ (F m <sup>-1</sup> )	$7 \times 10^{-10}$	Dielectric constant
$\phi, \phi_0$ (V)	1–6	Electric potential: $\mathbf{E} = -\nabla\phi$
$\psi$		Streamfunction, cf. (2.5)
$\rho, s$		Bulk charge and salt distribution
$\mathcal{P}$		Hydrodynamic pressure
$\rho_l$		Ionic liquid density

Table 1. Definitions of wavenumbers and parameter values.  $\rho$ ,  $k$ ,  $K$ ,  $\sigma$  and  $\kappa$  as in Ajdari (1995). Our  $k$  and  $K$  correspond to the  $q$  and  $Q$  of Ajdari (1995).  $p$  and  $\Delta$  correspond to the  $k$  and  $\delta$  of Landau & Lifshitz (1987, § 24) (replacing  $D$  with  $\nu$ ).

It is more convenient to replace (2.10) with a simpler expression. The same approximation that allowed the reduction of (2.3) into (2.4) leads the vanishing current condition (2.10) at the wall to become a boundary condition for the bulk charge  $\rho$ ,

$$\hat{\mathbf{n}} \cdot \nabla \rho = \kappa^2 \sigma, \quad \text{at a charged wall.} \tag{2.11}$$

Finally, appropriate conditions must be set at infinity if the domain is unbounded. We should stress here that the system of equations (the Poisson–Nernst–Planck system) (2.2) and (2.4) with the Neumann boundary conditions does not have a solution when  $k \equiv 0$ . Mathematically, the electric potential cannot satisfy all boundary conditions. However, the devices we have in mind are, say, at most 10 cm long, with a wavenumber  $k = 10 \text{ m}^{-1}$ . Past experiments on travelling wave electroosmosis employed electrode arrays with  $k \sim 10^4 \text{ m}^{-1}$  (Ramos *et al.* 2005) or even larger (Cahill *et al.* 2004). We will thus operate within the interval of physically realistic wavenumbers  $k \in (10^1, 10^5) \text{ m}^{-1}$ , as we stated in table 1.

The notation used in (2.8) implies that  $\rho$  and  $\phi$  are real fields. In the subsequent discussion, we will employ the same notation to denote complex fields from now on.

## 2.2. Velocity scales

We will employ the following velocity scales:

$$u_0 = \frac{1}{2} \frac{\sigma_0^2}{\epsilon \eta \kappa}, \quad u_1 = \frac{\epsilon \kappa \phi_0^2}{2\eta}, \quad (2.12)$$

and, where appropriate, define  $E \equiv \sigma_0/\epsilon$  to be the nominal electric field amplitude due to the interfacial charge distribution  $\sigma_0$  (Neumann problem). Here,  $\phi_0$  is a characteristic scale for the electric potential (Dirichlet problem). Dimensionless groups will be stated in raw form to avoid introducing new notation.

For brevity, we will use the phrases ‘Neumann velocities’ or ‘Dirichlet velocities’ to denote velocities obtained by solving the corresponding Poisson equation with Neumann or Dirichlet boundary conditions, respectively.

## 3. Boundary-driven flows in a semi-infinite space

We consider the configuration displayed in [figure 1](#). Travelling wave surface charges  $\sigma(x, t) = \sigma_0 e^{i(kx - \omega t)}$  are applied on the wall  $z = 0$  bounding a 1 : 1 electrolyte lying in the semi-infinite space  $z > 0$ . The boundary conditions satisfied by the bulk charge  $\rho$  and electric potential  $\phi$  at a solid surface lying at  $z = 0$  with the unit vector  $\hat{\mathbf{n}} = \hat{\mathbf{z}}$  are, from (2.9) and (2.11),

$$\partial_z \phi(x, z = 0, t) = -\frac{\sigma(x, t)}{\epsilon}, \quad \partial_z \rho(x, z = 0, t) = \kappa^2 \sigma(x, t). \quad (3.1)$$

Assuming  $\rho = \rho(z) e^{i(kx - \omega t)}$ , (2.7) reduces to  $\rho_{zz} + [i\omega/D - \kappa^2 - k^2]\rho = 0$ . To avoid clutter, we have introduced the notation  $\rho_z \equiv \partial_z \rho$  etc. Thus, the charge distribution reads

$$\rho(x, z, t) = -\frac{i\sigma_0 \kappa^2}{P} e^{i(Pz + kx - \omega t)}, \quad (3.2)$$

where we assumed a vanishing bulk charge at infinity and introduced the notation

$$P \equiv P_1 + iP_2 = \sqrt{p^2 - k^2 - \kappa^2}, \quad i\omega = Dp^2, \quad p = \frac{1+i}{\Delta}, \quad \Delta = \sqrt{\frac{2D}{\omega}}. \quad (3.3)$$

The notation employed in (3.3) for penetration depth  $\Delta$  and complex wavenumber  $p$  is analogous to that employed by Landau & Lifshitz (1987, p. 84). These quantities here, however, refer to the wave-like form of the charge distribution away from a charged boundary, rather than the wavelike form of the velocity field away from a no-slip wall. The penetration depth is now determined by the inverse of the imaginary part of  $P$  (taken here to be positive) and there is an oscillation whose wavevector is the real part of  $P$ . In other words, if  $P_1$  and  $P_2$  denote the real and imaginary parts of  $P$  in (3.3) ( $P = P_1 + iP_2$ ), where  $P_i$  are real and  $P_2 > 0$ , then

$$P_{1,2} = \frac{1}{\sqrt{2}} \sqrt{\sqrt{(\kappa^2 + k^2)^2 + \frac{\omega^2}{D^2}} \mp (\kappa^2 + k^2)}, \quad (3.4)$$

where the minus/plus sign corresponds to the real/imaginary part of  $P$ . Thus, the penetration depth is not determined by  $2\pi/\kappa$  but by the length scale  $2\pi/P_2 > 0$ . With this notation, the charge distribution has the form

$$\rho(x, z, t) = -\frac{i\sigma_0 \kappa^2}{P_1 + iP_2} e^{-P_2 z} e^{i(P_1 z + kx - \omega t)}. \quad (3.5)$$



Thus, in addition to the exponential decay away from the wall, there is a plane wave whose wavevector is not parallel to the surface charge distribution wave vector (it is not parallel to the  $x$ -axis) in (2.1) but lies in the direction  $k\hat{\mathbf{x}} + P_1\hat{\mathbf{z}}$ .

Similarly, assuming  $\phi = \phi(z)e^{i(kx - \omega t)}$ , (2.2) reduces to  $\phi_{zz} - k^2\phi = (i\sigma_0\kappa^2/\epsilon P)e^{iPz}$ , subject to the boundary condition (3.1) with surface charge (2.1) and  $\phi = 0$  at infinity (the alternative boundary condition of zero electric field at infinity leads to an identical result). Thus, the potential distribution reads

$$\phi(x, z, t) = \frac{\sigma_0}{\epsilon} \left( 1 + \frac{\kappa^2}{P^2 + k^2} \right) \frac{e^{-|k|z}}{|k|} e^{i(kx - \omega t)} + \frac{1}{\epsilon(P^2 + k^2)} \rho, \quad (3.6)$$

with  $\rho$  given by (3.5). Note that, as we mentioned in the previous section, setting  $k = 0$ , the boundary value problem does not have a solution since the electric potential  $\phi$  cannot satisfy both boundary conditions. This is then reflected in the divergence of expression (3.6) as  $k \rightarrow 0$ . For the purposes of this paper, however, where the physically realistic wavenumber  $k$  lies in the interval  $(10^1, 10^5) \text{ m}^{-1}$ , this limit is never attained.

Also, see Appendix A.2 for a comparison between the result (3.6) and its Debye–Hückel counterpart.

It is now clear that the nonlinear torque (last two terms in (2.8)) involves the harmonics  $e^{\pm i\theta}$  and  $e^{\pm 2i\theta}$ , where  $\theta = kx - \omega t$ , and the commensurate streamfunction  $\psi$  satisfying (2.8) will also be composed of the same harmonics. Thus, the velocity vanishes when averaged over the period  $2\pi/\omega$  of oscillations.

There is, however, a part of the nonlinear torque in (2.8) that is time-independent and does not vanish when averaged over the period of oscillations. This is caused by constructive interference of the various harmonics expressing the charge and potential distribution in (3.5) and (3.6), respectively, and gives rise to unidirectional pumping of liquid, its direction determined by the propagation direction of the charge distribution lying on the walls. We now investigate this zero mode.

Let  $\psi = \psi(z)$ , and thus the velocity  $\mathbf{v} = u(z)\hat{\mathbf{x}}$  as in (2.5), and consider both  $\psi$  and  $u$  to be real fields, cf. figure 1. In Appendix H.1, we show that after averaging over the period of oscillation, the vorticity equation (2.8) reduces to

$$\partial_z u(z) = \frac{i\epsilon k}{4\eta} (\phi^* \phi_z - \phi \phi_z^*), \quad (3.7)$$

where a star on  $\phi$  denotes the complex conjugate of (3.6). It is clear that the complex exponentials  $e^{i(kx - \omega t)}$  have cancelled out. This is the central formula of this paper. It states that the shear stress in a viscous electrolyte is given by the expression on the right-hand side (multiplied by viscosity) which resembles a probability current for a Schrödinger equation (Morse & Feshbach 1953). We also verify the validity of (3.7) by starting directly from the time-dependent Stokes equations, see Appendix H.2.

It is thus easy to determine the horizontal velocity component  $u(z)$ . Employing the complex form of the field  $\phi$  in (3.6), we solve (3.7) subject to the boundary conditions

$$u(z=0) = 0, \quad u(z=\infty) = \text{finite}. \quad (3.8)$$

Thus, the zero mode velocity  $u(z)$  from (3.7) with (3.6) becomes

$$u(z) = \frac{i\epsilon k}{4\eta} \int_0^z (\phi^* \phi_z - \phi \phi_z^*) dz. \quad (3.9)$$

The zero mode (3.9) inherits the boundary-layer structure of the field  $\phi$  as displayed in figure 2. A boundary layer of thickness  $O(P_2^{-1}) \sim \kappa^{-1}$  for large  $\kappa$  separates the no-slip region at the wall to the constant value acquired by the velocity away from the wall.

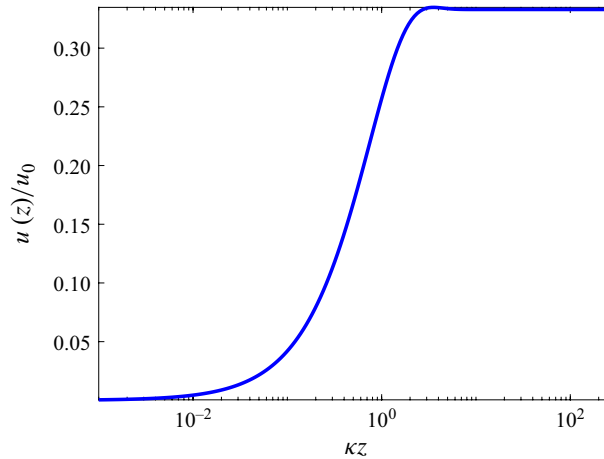


Figure 2. Boundary layer of thickness (= penetration depth, see (3.3)) of  $O(P_2^{-1}) \sim \kappa^{-1}$  for large  $\kappa$  employing (3.9). Beyond the boundary layer, the liquid velocity rapidly acquires a constant value.  $\kappa^{-1}$ ,  $D$ ,  $\eta$  are the Debye length, charge diffusion coefficient and liquid viscosity, respectively. Here, we have taken  $k = 10^5 \text{ m}^{-1}$ ,  $\kappa = 10^7 \text{ m}^{-1}$ ,  $D = 10^{-9} \text{ m}^2 \text{ s}^{-1}$  and  $\omega = D\kappa^2$ .  $u_0$  was defined in (2.12).

In the semi-infinite space formulation of the present section, the observable of interest is the value taken by the electrolyte velocity zero mode (3.9) at  $z = \infty$ . It reads

$$\frac{u(\infty)}{u_0} = \pm \frac{\kappa^3 (2R^3 \cos(3\Theta) - 4 \sin(2\Theta) R^2 |k| + 2R(\kappa^2 - k^2) \cos(\Theta) + \kappa^2 |k| \cot(\Theta))}{2R^2 (2R^2 k^2 \cos(2\Theta) - 4R|k|(R^2 + k^2) \sin(\Theta) - R^4 - 4R^2 k^2 - k^4)}, \quad (3.10)$$

where the plus sign gives the velocity for positive  $k$  and the negative sign for negative  $k$  and, following Ehrlich & Melcher (1982), the horizontal velocity  $u$  was scaled by  $u_0$ , cf. (2.12). Here,  $R$  and  $\Theta$  are the amplitude and phase of the complex wavenumber  $P = Re^{i\Theta}$  defined in (3.3) and given explicitly by

$$R = \left[ (\kappa^2 + k^2)^2 + \frac{\omega^2}{D^2} \right]^{\frac{1}{4}}, \quad \Theta = -\frac{1}{2} \arctan \left[ \frac{\omega}{D(\kappa^2 + k^2)} \right] + \frac{\pi}{2}. \quad (3.11)$$

In Appendix C, we discuss the relation of the velocity (3.10) with its counterpart that appeared in the past literature (Ehrlich & Melcher 1982).

### 3.1. Self-similar behaviour of the slip velocity

The zero mode slip velocity (3.10) displays a self-similar behaviour for the dimensions of the parameters  $\kappa$ ,  $k$ ,  $D$ ,  $\eta$ ,  $\omega$  define a matrix of rank three. Thus, there are two dimensionless combinations that can be formed (Bluman & Kumei 1989; Panton 1996). The average velocity (3.10) can then be expressed in the scaling form

$$u(z = \infty) = \frac{1}{2} \frac{\sigma_0^2}{\eta \epsilon \kappa} F \left( \frac{\omega}{D\kappa^2}, \frac{k}{\kappa} \right), \quad (3.12)$$

where  $F$  is a nonlinear function of the two independent dimensionless parameters and the front factor is the velocity scale  $u_0$  (2.12), as this is displayed in the vertical axis of figure 3.

In figure 3(a) we plot the ‘slip’ velocity (3.9), that is, the horizontal zero-mode velocity  $u(z)$  evaluated at  $z = \infty$  for various values of  $k$ . It is thus seen that all curves with  $k$  up to

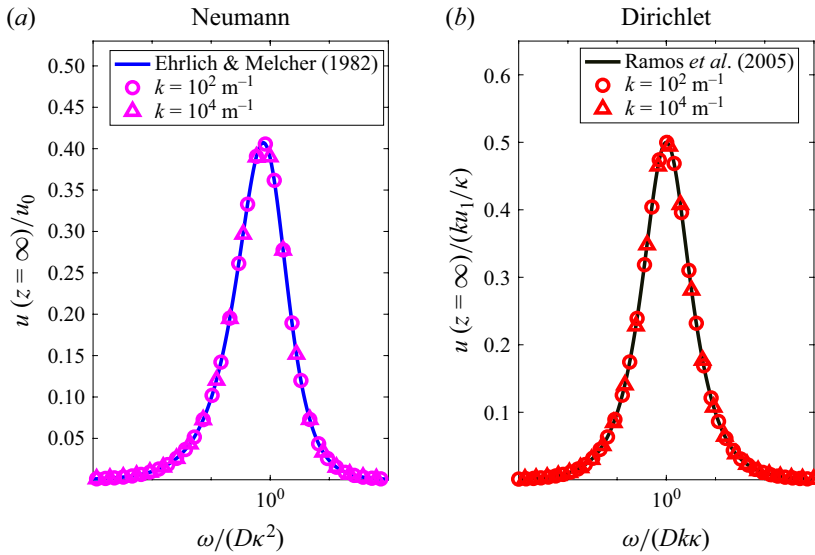


Figure 3. Horizontal zero-mode velocity evaluated at  $z = \infty$ , from (3.9) (a) as a function of dimensionless frequencies of the travelling wave wall charge and (b) as a function of the travelling electric potential at the wall, the latter was derived in Appendix F. The curves are self-similar as described by (3.12) and (3.13), based however on different dimensionless groups. Introducing the scaling that appears in the label of the vertical axis of panel (b), the Dirichlet results centre about the (continuous) curve introduced by Ramos *et al.* (2005), (10); (see (3.14)). The different  $k$  curves in panel (a) centre about the Ehrlich & Melcher (1982) expression, cf. (C2). If the value of  $k$  becomes sufficiently large, say  $k > 10^5 \text{ m}^{-1}$ , the amplitude of the curves in both panels decreases.

say  $10^5 \text{ m}^{-1}$  collapse into the single (continuous) curve introduced by Ehrlich & Melcher (1982), cf. (C2).

For comparison with results that have appeared in the more recent literature, in figure 3(b), we plot the velocity (3.9), but for Dirichlet boundary conditions, employing the potentials (F3), whose derivation was carried out in Appendix F. We thus display the slip velocity also in scaling form, although the dimensionless groups are now different,

$$u(z = \infty) = \frac{1}{2} \frac{\epsilon k \phi_0^2}{\eta} G \left( \frac{\omega}{Dk\kappa}, \frac{k}{\kappa} \right), \quad (3.13)$$

where  $G$  is a nonlinear function of the two dimensionless variables and the front factor is the velocity scale  $ku_1/\kappa$  (2.12), as this is displayed in the label of the vertical axis of figure 3(b). The curves appearing in figure 3(b) are thus the function  $G$  where we only vary its first argument. Notice that, had we employed  $\omega/(Dk^2)$  instead of  $\omega/(Dk\kappa)$  to non-dimensionalise  $u(\infty)$  in (3.13), the curves in figure 3(b) for each different  $k$  would be translated to the left and to the right of the centre curve.

All the curves in panel (b) collapse to the slip velocity (continuous curve) determined by Ramos *et al.* (2005), figure 10, having the form

$$u_{\text{Ramos}} = \frac{\kappa u_1}{k} \frac{\Omega}{1 + \Omega^2}, \quad (3.14)$$

where  $\Omega = \omega/(Dk\kappa)$  in our notation.

The self-similar behaviour of the velocity is important as it implies that results obtained with one experimental configuration can be employed to obtain estimates of results

corresponding to a different experimental configuration without the need to repeat the experiment.

### 3.2. Estimates of $u(\infty)$

The preceding discussion, although informative, it does not provide an understanding of the magnitude of the effects, which we thus analyse in the present section.

Let us obtain an estimate of the velocity  $u(\infty)$  in each case by considering the experimental values of Ramos *et al.* (2005) and García-Sánchez *et al.* (2006), where  $k \sim 10^4 \text{ m}^{-1}$ , voltage  $\phi_0 \sim 3 \text{ V}$  and employing standard parameter values for water  $\epsilon = 7 \times 10^{-10} \text{ F m}^{-1}$ ,  $\eta = 0.001 \text{ kg m}^{-1} \text{ s}$ ,  $\kappa = 10^7 \text{ m}^{-1}$ .

A fair comparison between figures 3(a) and 3(b) can be furnished by considering the dimensionless value of the velocity at the peak of the graph in each panel, which occurs at different frequencies. Thus, in the Dirichlet case, we consider  $\omega \sim Dk\kappa$ , thus giving the peak dimensionless velocity value  $\sim 0.5$  in figure 3(b), leading its dimensional counterpart to be equal to

$$u(\infty) = 1.57 \text{ cm s}^{-1} \quad (\text{Dirichlet}), \quad (3.15)$$

which is rather high. However, for the same values as above but adopting  $E = \sigma_0/\epsilon = 10^5 \text{ V m}^{-1}$ , as done by Ehrlich & Melcher (1982),  $\omega \sim D\kappa^2$ , thus giving the peak dimensionless velocity value of  $\sim 0.405$  in figure 3(a), leading its dimensional counterpart to be equal to

$$u(\infty) = 141 \text{ } \mu\text{m s}^{-1} \quad (\text{Neumann}), \quad (3.16)$$

which is within the order of magnitude of experimental velocities (cf. figure 7 of García-Sánchez *et al.* (2006), but also figures 2 and 10 of Cahill *et al.* (2004)). Note that the electric field varies on the length scale  $1/k$ , cf. (3.6), justifying the choice  $E = 10^5 \text{ V m}^{-1}$  for  $k \sim 10^4 \text{ m}^{-1}$ , in determining the estimate (3.16) for compatibility with the electric potential value  $\phi_0 \sim 3 \text{ V}$  employed in (3.15).

A recurrent theme in travelling wave electroosmosis studies is the high theoretical estimates (usually carried out by employing Dirichlet boundary conditions) in comparison to much lower, by a few orders of magnitude, experimental measurements (cf. Cahill *et al.* 2004; Ramos *et al.* 2005). It is thus possible that the Neumann boundary conditions employed in this paper and their accompanying estimates, as in (3.16), may resolve this inconsistency.

### 3.3. Tails of $u(\infty)$

Both Neumann and Dirichlet tails in figure 3 are of  $O(\omega)$  as  $\omega \rightarrow 0$ :

$$u(\infty) \sim \frac{\kappa \omega k(7k^2 + 8\kappa^2) + \sqrt{k^2 + \kappa^2}(8k^2 + 4\kappa^2)}{4D \left( \kappa^2 + 2k^2 + 2k\sqrt{k^2 + \kappa^2} \right)^2} \times \begin{cases} \frac{u_1}{k^2 + \kappa^2} & (\text{Dirichlet}), \\ \frac{u_0 \kappa^2}{(k^2 + \kappa^2)^2} & (\text{Neumann}), \end{cases} \quad \text{as } \omega \rightarrow 0. \quad (3.17)$$

The high-frequency asymptotics of the exact expressions (3.12) and (3.13) are given by

$$u(\infty) \sim \begin{cases} \frac{u_1}{\sqrt{2}} \left( \frac{k}{\kappa} \right)^{3/2} \left( \frac{\omega}{Dk\kappa} \right)^{-3/2} & (\text{Dirichlet}), \\ \frac{u_0}{\sqrt{2}} \left( \frac{\omega}{D\kappa^2} \right)^{-3/2} & (\text{Neumann}), \end{cases} \quad \text{as } \omega \rightarrow \infty. \quad (3.18)$$

Notice that the inherent frequency scalings in (3.18) agree with the scalings of the functions  $G$  and  $F$  in (3.13) and (3.12), respectively.

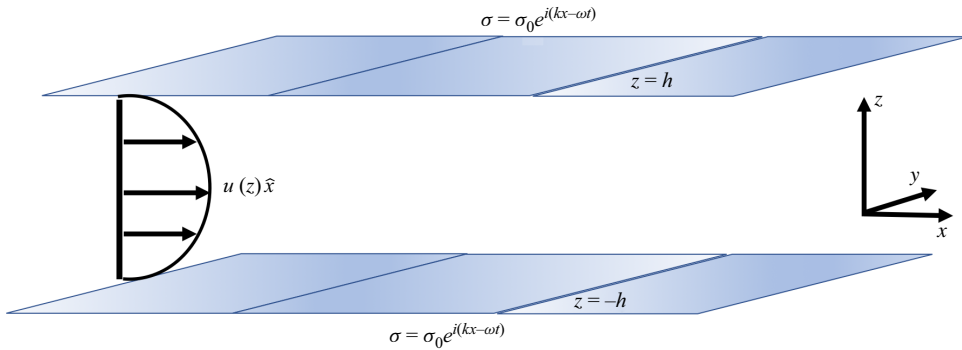


Figure 4. Travelling wave wall charges give rise to a nonlinear body force and torque (see (2.8)) in a 1 : 1 electrolyte in a rectangular channel of width  $2h$  leading to the appearance of a (zero mode) unidirectional fluid velocity in the  $\hat{x}$  direction, parallel to the channel walls that is quadratic with respect to the associated electric field and that does not vanish after averaging over the charge period of oscillation.

#### 4. Boundary-driven flows in a channel of width $2h$

It is more physically realistic to consider the configuration displayed in figure 4. Travelling wave surface charges are applied on the channel walls at  $z = \pm h$  enclosing a 1 : 1 electrolyte. The boundary conditions satisfied by the potential  $\phi$  and by the charge  $\rho$  are

$$\partial_z \phi(x, z = \pm h, t) = \pm \frac{\sigma(x, t)}{\epsilon}, \quad \partial_z \rho(x, z = \pm h, t) = \mp \kappa^2 \sigma(x, t), \quad (4.1)$$

with  $\sigma = \sigma_0 e^{i(kx - \omega t)}$ . The choice of this set-up was dictated by results showing that the ideal and optimal configuration seems to require symmetrical electrode arrays with respect to the channel centre and with no phase lag between them (Yeh *et al.* 2011).

Assuming  $\rho = \rho(z) e^{i(kx - \omega t)}$  and subject to the boundary condition (4.1) with surface charge (2.1), the equations to solve are identical to those of the semi-infinite space. Thus, the charge distribution reads

$$\rho(x, z, t) = \frac{\sigma_0 \kappa^2 \cos Pz}{P \sin Ph} e^{i(kx - \omega t)}, \quad (4.2)$$

where  $P$  is the complex wavenumber defined in (3.3).

Similarly, assuming  $\phi = \phi(z) e^{i(kx - \omega t)}$  and subject to the boundary condition (4.1) with surface charge (2.1), the potential distribution reads

$$\phi(x, z, t) = \frac{\sigma_0}{\epsilon} \left( 1 + \frac{\kappa^2}{P^2 + k^2} \right) \frac{\cosh kz}{k \sinh kh} e^{i(kx - \omega t)} + \frac{1}{\epsilon(P^2 + k^2)} \rho, \quad (4.3)$$

with  $\rho$  given by (4.2). We note that, as is the case in the semi-infinite space, the above equations do not have a solution when  $k = 0$ . For the same reasons as before, we are not interested in this limit as the physically realistic wall charge excitation wavenumbers we have in mind are very large, lying in the interval  $(10^1, 10^5) \text{ m}^{-1}$ , as is stated in table 1.

The zero-mode velocity in the channel again satisfies the integrated momentum (3.7). Employing the complex form of the field  $\phi$  in (4.3), we thus solve (3.7) subject to the no-slip boundary conditions

$$u(z = \pm h) = 0. \quad (4.4)$$

The zero-mode velocity  $u(z)$  from (3.7) with (4.3) becomes

$$u(z) = \frac{i\epsilon k}{4\eta} \int_h^z (\phi^* \phi_z - \phi \phi_z^*) dz. \quad (4.5)$$

This is essentially a plug-like flow with very thin boundary layers of thickness  $\sim \kappa^{-1}$  located at  $z = \pm h$ . The exact form of (4.5) is delegated to [Appendix E \(E3\)](#). The meaningful observable here is the average value of the zero mode over the width of the channel

$$\langle u \rangle = \frac{1}{2h} \int_{-h}^h u(z) dz. \quad (4.6)$$

As it stands, (4.6) is a double integral and could be awkward to evaluate, especially in cylindrical polars (see § 5). It can be significantly simplified by changing the order of integration and carrying out one of the integrations. It can thus be written as a single integral in the form

$$\langle u \rangle = -\frac{1}{2h} \frac{i\epsilon k}{4\eta} \int_{-h}^h (\phi^* \phi_z - \phi \phi_z^*) z dz, \quad (4.7)$$

where the parity of  $\phi$  with respect to the origin  $z = 0$  was taken into account. The exact form of (4.6) is delegated to [Appendix E \(E5\)](#).

#### 4.1. Self-similar behaviour of the average velocity in the channel

The zero-mode velocity (4.7) displays a self-similar behaviour for the dimensions of the available parameters  $h, \kappa, k, D, \eta, \omega$  define a matrix of rank three. From the available dimensionless combinations (Bluman & Kumei 1989; Panton 1996), we display the following in the average velocity (4.6):

$$\langle u \rangle = \frac{1}{2} \frac{\sigma_0^2}{\eta \epsilon k} f\left(\frac{\omega}{D\kappa^2}, \kappa h\right), \quad (4.8)$$

where  $f$  is a nonlinear function of the two independent dimensionless parameters and the front factor is the velocity scale  $\kappa u_0/k$ , cf. (2.12), as this is displayed in the label of the vertical axis of [figure 5](#) (the scaling theory allows other combinations as well, for instance, see (4.14) below). The front factor in (4.8) implies that  $\langle u \rangle$  scales as  $k^{-1}$ . This behaviour is clearly displayed by the continuous curve in [figure 14\(b\)](#) of [Appendix G](#). Such a behaviour for Neumann boundary conditions was met before (Liu *et al.* 2018, figure 6f). Therein, increasing the size of the system gave rise to a commensurate increase of the Coulomb force and the resulting slip velocity. The curve in figure 6(f) of this reference has exactly slope equal to 1, that is, the slip velocity scales linearly with respect to system size, and is thus inversely proportional to  $k$ , as this is demonstrated by the front factor in (4.8) and the continuous curve in [figure 14\(b\)](#).

A good single-parameter fit of these results that accounts for all dimensionless frequencies, including those present in the tails, is given by the continuous line in [figure 5\(a\)](#) and has the functional form

$$\langle u \rangle_{E\&M} = \frac{\beta}{\kappa h} \frac{\frac{\omega}{D\kappa^2}}{\left[\left(\frac{\omega}{D\kappa^2}\right)^2 + 1\right]^{\frac{5}{4}}} \cos\left(\frac{\arctan\left(\frac{\omega}{D\kappa^2}\right)}{2}\right), \quad (4.9)$$

i.e. it is the velocity (C2) scaled accordingly and the single-parameter value  $\beta = 0.926$ .



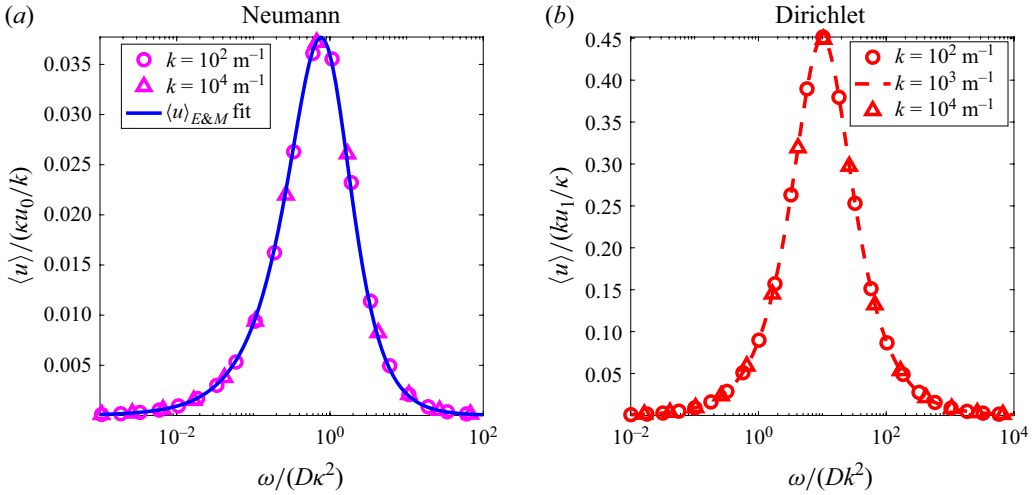


Figure 5. Self-similar behaviour of the zero mode velocity (4.6), averaged over the channel width  $2h$  as a function of dimensionless frequencies (a) of the travelling wave wall charge or (b) of the travelling electric potential at the wall, the latter was derived in Appendix F. The curves are self-similar as described by relations (4.8) and (4.10). We emphasise that the dimensionless group  $\omega/(Dk^2)$  employed in panel (b) differs from the group  $\omega/(D\kappa^2)$  employed in panel (a), and furthermore, it is different to the group  $\omega/(Dk\kappa)$  employed for the Dirichlet case in the semiinfinite space (figure 3b). In both panels,  $h = 10^{-5}$  m,  $D = 10^{-9}$  m<sup>2</sup> s<sup>-1</sup> and in panel (a), we employed the fit (4.9) with the single parameter  $\beta = 0.926$ .

Thus, experimental results obtained by employing a single configuration that agree with the above behaviour can be extrapolated theoretically to fit alternative experimental conditions and parameters without the need of repeating the experiments.

Employing the Dirichlet boundary conditions instead, we obtain the potential (F6) and thus the velocity (4.7) acquires the self-similar form

$$\langle u \rangle = \frac{1}{2} \frac{\epsilon k \phi_0^2}{\eta} g\left(\frac{\omega}{Dk^2}, \kappa h\right), \quad (4.10)$$

where  $g$  is a nonlinear function of the two independent dimensionless parameters and the front factor is the velocity scale  $\kappa u_1 / \kappa$  cf. (2.12), as this is displayed in the vertical axis of figure 5(b). Notice however that the dimensionless group  $\omega/(Dk^2)$  employed in (4.10) (figure 5b) differs from the group  $\omega/(D\kappa^2)$  employed in (4.8) (figure 5a) and furthermore, it is different to the group  $\omega/(Dk\kappa)$  employed for the Dirichlet case in the semiinfinite space in (3.13) (figure 3b).

#### 4.2. Average velocity $\langle u \rangle$ estimates

We estimate the channel average velocity by considering the same material parameters as in § 3.2. Comparison between figures 5(a) and 5(b) can be furnished by considering the dimensionless value of the velocity at the peak of the graph in each panel, which occurs at different frequencies. In the Dirichlet case, we consider  $\omega \sim Dk^2$ , thus giving the peak dimensionless velocity value of  $\sim 0.45$  in figure 5(b), leading its dimensional counterpart to equal

$$\langle u \rangle = 1.4 \text{ cm s}^{-1} \quad (\text{Dirichlet}). \quad (4.11)$$

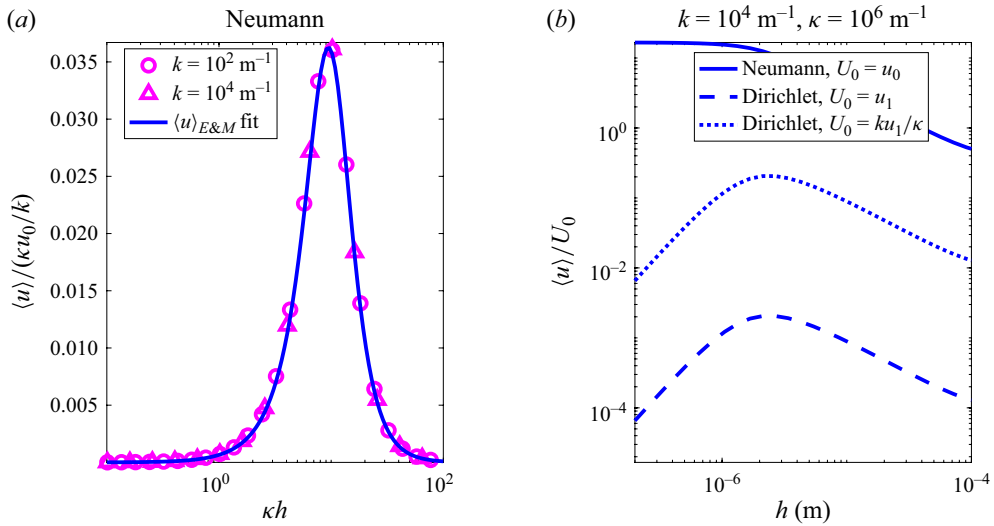


Figure 6. (a) Self-similar behaviour of average velocity by varying only the scaled channel width (second argument of (4.8)). Continuous line denotes the fit (4.9). (b) Averaged channel width zero mode velocity (4.7) versus channel height  $h$ , obtained with Neumann or Dirichlet boundary conditions (employing the potentials (4.3) and (F6), respectively) and scaled by either  $u_0$ ,  $u_1$  or  $\kappa u_1 / k$  (cf. (2.12)). The Neumann velocity reaches a plateau for small channel heights, while its Dirichlet counterpart decays to zero. For larger values of  $h$ , all curves reach plateaus. Curves obtained with a frequency corresponding to the peak velocity of figures 5(a) and 5(b), respectively.

However, for the same values as above but adopting  $E = 10^5 \text{ V m}^{-1}$ , as done by Ehrlich & Melcher (1982),  $\omega \sim D\kappa^2$ , thus giving the peak dimensionless velocity value of  $\sim 0.037$  in figure 5(a), leading its dimensional counterpart to equal

$$\langle u \rangle = 1.3 \text{ cm s}^{-1} \quad (\text{Neumann}), \quad (4.12)$$

which are comparable to each other. Notice however that the velocity scaling of the Dirichlet problem  $\kappa u_1 / k$  decreases linearly with increasing  $k$  and that the Neumann scaling  $\kappa u_0 / k$ , increases, cf. labels of the vertical axes of figures 5(a) and 5(b), respectively.

#### 4.3. Average velocity $\langle u \rangle$ asymptotic behaviour

In figure 6, we display the characteristic behaviour of the average velocity (4.7) as the height  $h$  of the channel varies. The Neumann velocity in general increases as  $h$  decreases reaching a plateau at small channel heights (where the Debye layers from adjacent walls start to overlap). The Dirichlet velocity decays to zero in this limit. These behaviours are described by the limiting expressions

$$\langle u \rangle \sim \begin{cases} \frac{\kappa u_1}{\kappa} \frac{\frac{\omega}{Dk^2}}{3 \left[ 1 + \left( \frac{\omega}{Dk^2} \right)^2 \right]} (\kappa h)^2 & (\text{Dirichlet}), \\ \frac{\kappa u_0}{k} \frac{2}{3} \frac{-\kappa^2 P_1 P_2 [P_1^2 + (P_2 + k)^2]^3 [P_1^2 + (P_2 - k)^2]^3}{|P|^4 [P^2 + k^2]^3 [(P^*)^2 + k^2]^3} & (\text{Neumann}), \end{cases} \quad \text{as } h \rightarrow 0,$$

where  $P$  is defined in (3.3), and  $u_0$  and  $u_1$  in (2.12). Combination of this result with the  $k$  scaling behaviour, displayed in figure 14, leads to the conclusion that the Neumann conditions provide prominent average velocities in thin and long channels (where the wavelength of the charge excitation at the walls can become sufficiently long).

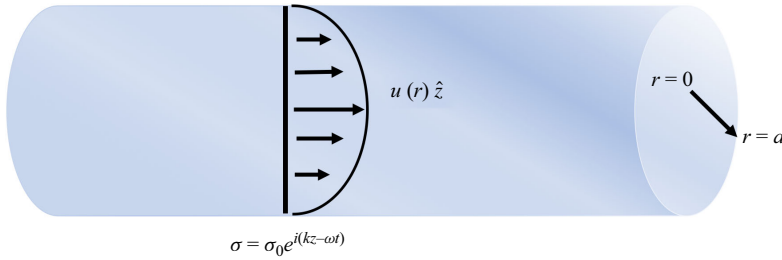


Figure 7. Travelling wave wall charges give rise to a nonlinear body force and torque (see (2.8)) in a 1 : 1 electrolyte in a cylindrical capillary of radius  $a$  leading to the appearance of a unidirectional fluid velocity in the  $\hat{z}$  direction, along the capillary centre axis, that is quadratic with respect to the associated electric field and that does not vanish after averaging over the charge period of oscillation.

Both Neumann and Dirichlet tails in figure 5 are of  $O(\omega)$  (whose coefficients are too long to include here), as  $\omega \rightarrow 0$ . The high-frequency asymptotics of the exact expressions (4.8) and (4.10) are given by

$$\langle u \rangle \sim \begin{cases} u_1 \frac{1}{\sqrt{2}} \left( \frac{\omega}{Dk^2} \right)^{-3/2} \tanh kh \text{ (Dirichlet),} \\ \frac{u_0}{\sqrt{2} \tanh kh} \left( \frac{\omega}{Dk^2} \right)^{-3/2} \text{ (Neumann),} \end{cases} \quad \text{as } \omega \rightarrow \infty. \quad (4.14)$$

It is clear that the expressions in (4.14) justify the frequency scalings of the functions  $g$  and  $f$  in (4.10) and (4.8), respectively.

## 5. Boundary-driven flows in a cylindrical capillary

A still more physically realistic configuration is displayed in figure 4. Travelling wave surface charges  $\sigma = \sigma_0 e^{i(kz - \omega t)}$  are applied to the wall of a capillary with circular cross-section of radius  $a$ , enclosing a 1 : 1 electrolyte. The boundary conditions satisfied by the potential  $\phi$  and by the charge  $\rho$  are

$$\partial_r \phi(z, r = a, t) = \frac{\sigma(z, t)}{\epsilon}, \quad \partial_r \rho(z, r = a, t) = -\kappa^2 \sigma(z, t), \quad (5.1)$$

and we take the axis of the cylinder to lie in the  $z$ -direction as displayed in figure 7. Assuming  $\rho = \rho(r) e^{i(kz - \omega t)}$  and  $\phi = \phi(r) e^{i(kz - \omega t)}$ , the evolution equation for the charge and Gauss law reduce to

$$\rho_{rr} + \frac{1}{r} \rho_r + \left[ \frac{i\omega}{D} - k^2 - \kappa^2 \right] \rho = 0 \quad \text{and} \quad \phi_{rr} + \frac{1}{r} \phi_r - k^2 \phi = -\frac{\rho}{\epsilon}, \quad (5.2)$$

respectively. With boundary conditions (5.1), we obtain

$$\rho(z, r, t) = \frac{\sigma_0 \kappa^2 J_0(Pr)}{P J_1(Pa)} e^{i(kz - \omega t)}, \quad (5.3)$$

where  $P$  is (again) the complex wavenumber (3.3) and  $J_0, J_1$  are Bessel functions of the first kind. Likewise, subject to the boundary condition (5.1), the potential distribution reads

$$\phi(z, r, t) = \frac{\sigma_0}{\epsilon} \left( 1 + \frac{\kappa^2}{P^2 + k^2} \right) \frac{I_0(kr)}{k I_1(ka)} e^{i(kz - \omega t)} + \frac{1}{\epsilon(P^2 + k^2)} \rho, \quad (5.4)$$

with  $\rho$  given by (5.3), and  $I_0$  and  $I_1$  are modified Bessel functions of the first kind (Bessel functions of imaginary argument).

As before, the velocity field consists of terms that vanish after averaging over the period of oscillation of the fields. The exception is the zero-mode velocity, satisfying an equation analogous to (3.7). Starting from the time-dependent Stokes equations and considering the velocity field to have the form  $\mathbf{v} = u(r)\hat{\mathbf{z}}$  (as depicted in figure 7), we obtain

$$u_{rr} + \frac{1}{r}u_r + \frac{ik}{4\eta}(\rho\phi^* - \rho^*\phi) = 0. \quad (5.5)$$

Using the second of (5.2) and performing one integration, we arrive at

$$\partial_r u(r) = \frac{i\epsilon k}{4\eta}(\phi^*\phi_r - \phi\phi_r^*), \quad (5.6)$$

which is the cylindrical counterpart of (3.7). Employing the complex form of the field  $\phi$  in (5.4), we thus solve (5.6) subject to the no-slip boundary condition

$$u(r=a) = 0. \quad (5.7)$$

The zero-mode velocity  $u(r)$  from (5.6) with (5.4) becomes symbolically

$$u(r) = \frac{i\epsilon k}{4\eta} \int_a^r (\phi^*\phi_r - \phi\phi_r^*) dr, \quad (5.8)$$

which is the cylindrical counterpart of (3.9) and (4.5) (the constant of integration is zero to maintain  $\partial_r u|_{r=0} = 0$ ). Otherwise, the flow would have a cusp (discontinuous derivative of  $u$ ) at  $r=0$ ). The same steps followed in the semi-infinite space problem of § 3 lead to a long expression for  $u(r)$  which is a plug-like flow with very thin boundary layers of thickness of  $\sim \kappa^{-1}$  located at the cylinder wall  $r=a$ . The meaningful observable here is the average value of the zero mode over the capillary cross-sectional area, defined as

$$\langle u \rangle = \frac{1}{\pi a^2} \int_0^a u(r) 2\pi r dr, \quad (5.9)$$

where  $u(r)$  is given by (5.8). Equation (5.9) is a double integral and involves integrals of Bessel function pairs which, in general, cannot be calculated in closed form (for exceptions, see for instance Luke (1962)). We circumvent this complication by exchanging the order of integration in the double integral appearing in (5.9). Thus, (5.9) can be written as a single integral

$$\langle u \rangle = \frac{-1}{a^2} \frac{i\epsilon k}{4\eta} \int_0^a (\phi^*\phi_r - \phi\phi_r^*) r^2 dr, \quad (5.10)$$

and is calculated numerically by simple quadrature. In figure 8, we display the zero mode velocity averaged over the channel width (5.10) versus the frequency of charge oscillation  $\omega$  scaled by the frequency  $D\kappa^2$ , where  $D$  is the diffusion coefficient of the charge distribution.

### 5.1. Self-similar behaviour of the average velocity in the cylindrical capillary

The zero mode velocity (5.10) displays a self-similar behaviour for the same reason discussed in the channel case. From the available dimensionless combinations (Bluman & Kumei 1989; Panton 1996), we display the following in the average velocity (5.10):

$$\langle u \rangle = \frac{1}{2} \frac{\sigma_0^2}{\eta\epsilon k} \mathcal{F}\left(\frac{\omega}{D\kappa^2}, \kappa a\right), \quad (5.11)$$

where  $\mathcal{F}$  is a nonlinear function of the two independent dimensionless parameters and the front factor is the velocity scale  $\kappa u_0/k$  cf. (2.12), as this is displayed in the label of the

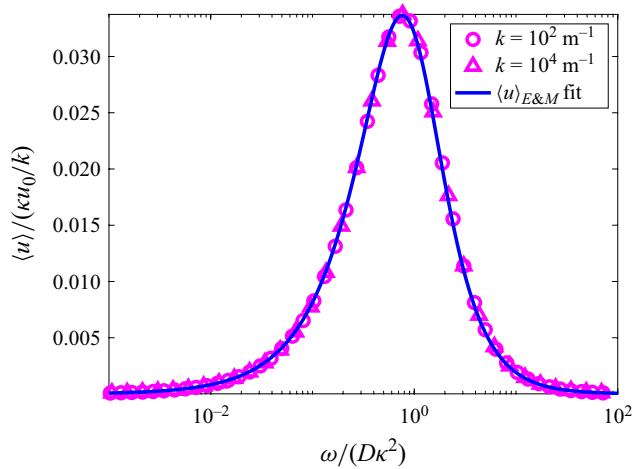


Figure 8. Average velocity in a cylinder, cf. figure 7, with travelling wave charge distribution (that is, Neumann boundary conditions for the Poisson equation). Self-similar behaviour of the zero mode velocity (5.9), averaged over the cross-sectional area of the cylinder of radius  $a$  as a function of the dimensionless frequency  $\omega/(D\kappa^2)$  of the travelling wave wall charge. The curves are self-similar as described by relation (5.11). Continuous line denotes the fit (5.12) by adopting the single-parameter value  $\beta = 1.9$ .  $a = 10^{-5}$  m,  $D = 10^{-9}$  m<sup>2</sup> s<sup>-1</sup>.

vertical axis of figure 8. A good single-parameter fit of these results that accounts for all parameter values, including the tails in figure 8, has the functional form

$$\langle u \rangle_{E\&M} = \frac{\beta}{\kappa a} \frac{\frac{\omega}{D\kappa^2}}{\left[ \left( \frac{\omega}{D\kappa^2} \right)^2 + 1 \right]^{\frac{5}{4}}} \cos \left( \frac{\arctan \left( \frac{\omega}{D\kappa^2} \right)}{2} \right), \quad (5.12)$$

i.e. it is the velocity (C2) scaled accordingly and we have adopted the single-parameter value  $\beta = 1.9$  in figure 8. In figure 8, we plot the function  $\mathcal{F}$  from (5.11) versus the dimensionless (Debye) frequency for a number of values of the excitation wavenumber  $k$ .

We estimate the cylinder average velocity by considering the same material parameters as in § 3.2. Adopting  $E = 10^5$  V m<sup>-1</sup>, as done by Ehrlich & Melcher (1982),  $\omega \sim D\kappa^2$ , thus giving the peak dimensionless velocity value of  $\sim 0.0715$  in figure 8, leading its dimensional counterpart to equal

$$\langle u \rangle = 2.5 \text{ cm s}^{-1}. \quad (5.13)$$

Notice, however, that this estimate decreases with increasing  $k$ .

## 6. Numerical results

In this section, we solve the Poisson–Nernst–Planck–Navier–Stokes differential equations numerically with a finite-element package (Comsol). We are interested in establishing the existence of the zero mode velocity and how does it compares in magnitude and its general trend with the exact solutions obtained in the previous section.

We employ the cylindrical capillary geometry of § 5 amended so as to incorporate effects of boundaries in the longitudinal direction of the cylinder as displayed in figure 9 and explained in more detail in the supplementary materials addendum. We employ the low-Péclet-number approximation to the Poisson–Nernst–Planck–Navier–Stokes

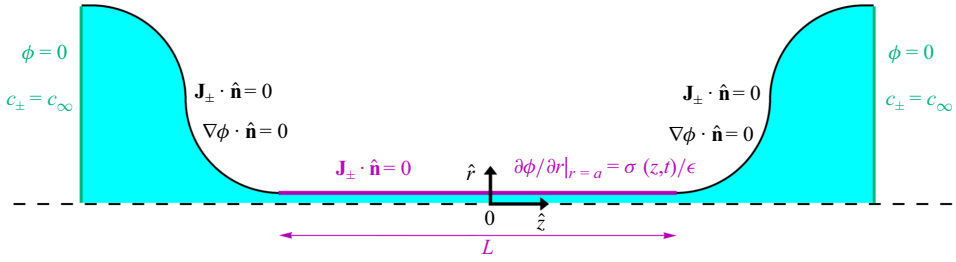


Figure 9. Configuration of the domain for the numerical solution of the Poisson–Nernst–Planck–Navier–Stokes system in § 6.

differential equations which, for the material parameters employed in this paper, is a valid approximation as shown in [Appendices B.1](#) and [B.2](#).

Numerically, we solve the full Poisson–Nernst–Planck–Navier–Stokes system and obtain the species distributions, electric field and velocity, without other approximations. For instance, the time-dependent Stokes equations read

$$\rho_l \frac{\partial \mathbf{v}}{\partial t} = -\nabla p + \eta \nabla^2 \mathbf{v} + \rho \nabla \phi, \quad \nabla \cdot \mathbf{v} = 0. \quad (6.1)$$

The set-up of the system is shown in [figure 9](#). The cylinder has length  $L$  and is connected to two reservoirs of fixed charge concentration and zero electric potential (left-most and right-most edges of the figure). The boundary conditions in the lateral surface of the cylinder are the same as those employed in § 5 of the manuscript and we employ the real part of the wall charge density (thus,  $\sigma(z, t) = \sigma_0 \cos(kz - \omega t)$ ). The intermediate regions connecting the two reservoirs to the cylinder have boundary conditions of zero normal electric field and zero normal current  $\hat{\mathbf{n}} \cdot \mathbf{J}_{\pm}$ , where

$$\mathbf{J}_{\pm} = -D \left[ \nabla c_{\pm} \pm \frac{e}{k_B T} c_{\pm} \nabla \phi \right] \quad (6.2)$$

and  $\hat{\mathbf{n}}$  is the normal vector to the interface. We employ the parameters

$$\begin{aligned} a &= 10^{-5} \text{ m}, \quad L = 2 \times 10^{-4} \text{ m or } L = 4 \times 10^{-4} \text{ m}, \quad D = 10^{-9} \text{ m}^2 \text{ s}^{-1}, \\ \sigma_0 &= 7 \times 10^{-5} \text{ C m}^{-2}, \quad \kappa = 2.3 \times 10^6 \text{ m}^{-1}, \quad k = 0.8 \times 10^5 \text{ m}^{-1}, \\ 2c_{\infty} &= 10^{-3} \text{ mM}. \end{aligned} \quad (6.3)$$

To obtain the zero mode, we average the time-dependent velocity field over the cylinder cross-section, the cylinder length  $L$  (cf. [figure 9](#)) and over  $N$  periods of oscillation of the applied field, where  $N$  is an integer. The details are described in the supplementary materials addendum.

The circle and triangle symbols in [figure 10\(a\)](#) denote the velocity obtained numerically with the configuration of [figure 9](#) and parameters (6.3). In general, there is excellent agreement with the exact solution (5.9) (continuous curve) at the tails. Away from the latter, the numerical and exact results agree well in an order-of-magnitude basis and share the same general trend.

The difference seen between the averaged zero-mode velocity obtained numerically here and the exact model, as seen in [figure 10\(a\)](#), can mostly be attributed to the requirement of finite length geometry for the numerical configuration. Indeed, we have verified that by increasing  $L$ , the numerical results approach their analytical counterparts as can be seen by comparison of the circle and triangle data points in [figure 10\(a\)](#) with its exact counterparts. One explanation for this behaviour is that small length  $L$  of the capillary tube is mainly



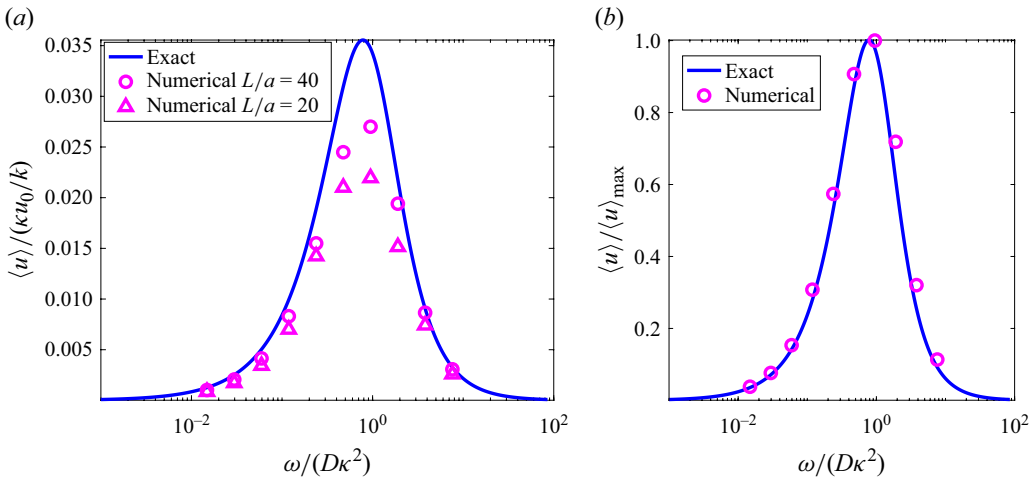


Figure 10. (a) Comparison of the exact zero mode velocity (5.9) (continuous curve, calculated with a cylinder of infinite length) with two of its numerical counterparts (circles and triangles) obtained with the finite-element package Comsol in the geometry displayed in figure 9 by employing the parameter values (6.3) (with cylinder aspect ratio  $L/a = 20$  and  $L/a = 40$ ). In general, the agreement between the exact and the numerical results is very good near the tails. The difference between numerical and exact solutions is attributed to hydrodynamic entrance and edge effects when the aspect ratio  $L/a$  is relatively small. As the aspect ratio  $L/a$  increases, however, the numerical solution converges to the exact as seen by comparing the circle with the triangle data points. (b) Following figure 10(b) of Cahill *et al.* (2004), we display the same data points/continuous curve as in panel (a) but now dividing the velocities by their maximum value. In general, the agreement between exact and numerical results is excellent.

associated with a hydrodynamic entrance flow and edge effects, while the analytical result assumes that the flow is maintained in a domain of infinite length. Figure 10 is generated by employing the parameter values (6.3), where the tube aspect ratio (length-to-radius) is  $L/a = 20$  and  $L/a = 40$ . In the supplementary materials addendum, we provide the corresponding data tables. A full parametric analysis of travelling wave electroosmosis in a finite-length capillary tube is beyond the scope of this paper.

Finally, following figure 10(b) of Cahill *et al.* (2004), we compare the exact and numerically obtained zero-mode velocities by scaling each one of the curves in figure 10(b) by their respective maximum. Now, there is an excellent agreement between the exact and the numerically obtained zero mode velocities as displayed in figure 10(b).

In the supplementary materials addendum, we briefly discuss the effect a finite Péclet number has on the velocity magnitude.

## 7. Discussion

The key figures 3(b) and 5(b) show that scalings required for the Dirichlet problem to bring the velocity in self-similar form differ between the semi-infinite space and the channel. In addition, the frequency dimensionless groups depend on the wavenumber  $k$  of the excitation at the wall. However, figures 3(a) and 5(a) (and their accompanying scaling forms (3.12) and (4.8), both obtained with Neumann boundary conditions for the Poisson equation) show that the excitation frequency  $\omega$  is scaled by its Debye counterpart  $D\kappa^2$  that is independent of the excitation wavelength and does not depend on geometry considerations. This latter quality might make Neumann boundary conditions to be preferable to their Dirichlet counterparts in modelling travelling wave electroosmosis-related effects as was already pointed out in the literature of electrokinetic energy

conversion and its efficiency in nanofluidic channels by matching theory (van der Heyden *et al.* 2006) with experiment (van der Heyden *et al.* 2007).

Along with our theory, we provided the simple single-parameter fits  $\langle u \rangle_{E\&M}$  (see (4.9) and (5.12)) which can be employed as a rapid test of consistency between our theory and future travelling wave electroosmosis experiments.

The Neumann velocities increase with decreasing channel width  $h$ , reaching a plateau, cf. the continuous curve in figure 6(b). The Dirichlet velocities, however, after reaching a maximum, decay to zero as  $h \rightarrow 0$ , see the dashed lines in figure 6(b) and the exact expression (4.13). Likewise, the velocity becomes more pronounced when the excitation wavelength increases, cf. Appendix G and figure 6(f) of Liu *et al.* (2018). These geometrical realisations may have consequences on how an experiment is designed.

The velocity estimates we obtain, by employing Neumann boundary conditions for the Poisson equation, seem to be within the purview of experimental measurements, at least in an order-of-magnitude basis. We were currently unable to exactly match the available experimental results with our theory. We believe however that this can be done in a future contribution after carefully selecting the boundary conditions the Poisson equation satisfies at a wall.

The numerical simulations we performed with the finite-element package Comsol for the configuration displayed in figure 9 and described in § 6 and the supplementary materials addendum, demonstrate the consistency in order-of-magnitude, and general trend between the exact zero mode velocity and its numerically obtained counterpart, despite the finiteness of the configuration employed in the latter. Of course, the displayed numerical results can be calibrated by changing parameters and conditions (e.g. by setting the electric field to be zero in the reservoirs or setting up periodic boundary conditions) and can be generalised by including the effect the advective terms in the Nernst–Planck equation have on the zero mode.

The formulae describing the observable of interest here, that is, the liquid velocity in (4.5) and (5.8), are general and can thus be adopted to different configurations than those employed here. This is attained by solving the commensurate electric problem with alternative boundary conditions and using the provided velocity formulae for the ‘slip’ (3.10) and average velocities (4.7) and (5.10) in the main body of this article ‘as is’.

In general, the zero mode velocity is attributed to the invariance of the equations of motion (see for instance the vorticity equation (2.8)) under  $SO(2)$  rotations in the  $x$ – $z$  plane (in the channel case) or  $z$ – $r$  plane (in the cylindrical capillary case), and the presence of mean-field solutions that can be parametrised by the elements of the invariance group. Quadratic fluctuations of these mean field solutions give rise to a longitudinal mode that costs finite energy to change their magnitude, and to a zero mode costing no energy in the long wavelength limit. See Negele & Orland (1988, pp. 214–219) for a detailed discussion.

Finally, we note that the existence and regularity of solutions to the Nernst–Planck–Navier–Stokes system for Dirichlet boundary conditions in an infinite periodic channel or with time dependence (and so similar to the configuration and conditions employed here, but not identical) was recently established by Constantin *et al.* (2021, 2022).

**Supplementary material.** Supplementary material is available at <https://doi.org/10.1017/jfm.2025.288>.

**Acknowledgements.** The authors are grateful to three anonymous referees for comments and suggestions that improved the manuscript.

**Funding.** This work was supported by the US National Science Foundation through the Northwestern University MRSEC grant number DMR-2308691.

**Declaration of interests.** The authors report no conflict of interest.

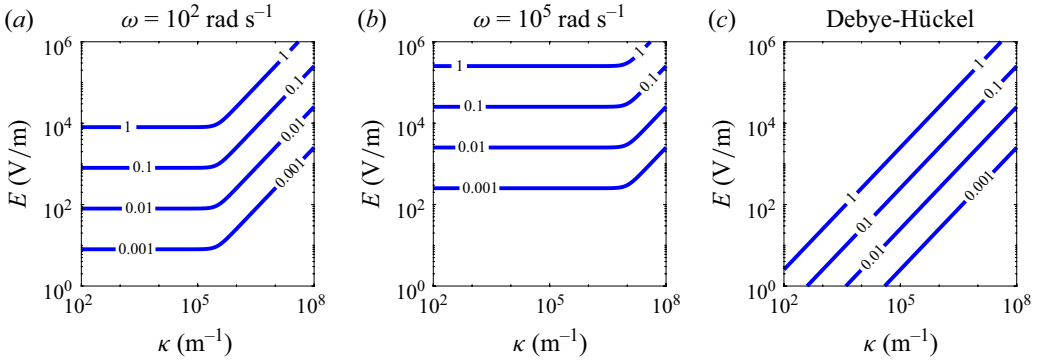


Figure 11. (a,b) Validity of the charge perturbation approximation employed in this paper (contours of the function  $f(\kappa, E)$  in (A2)) and (c) Debye–Hückel approximation (contours of the function  $eE/\kappa k_B T$  in (A4)). The plateau in panels (a) and (b) is due to the frequency renormalisation of the Debye wavenumber  $\kappa$  in the denominator of (A2). It is thus seen that the range of validity of the approximation increases as the frequency  $\omega$  (or the ratio  $\omega/D$ ) increases. Here,  $k = 10^5 \text{ m}^{-1}$ , and  $D = 10^{-9} \text{ m}^2 \text{ s}^{-1}$  at room temperature.

## Appendix A. Debye–Falkenhagen approximation

### A.1. Validity of the Debye–Falkenhagen perturbation approximation

We are unaware of a study in the literature examining the range of validity of the Debye–Falkenhagen approximation. It is thus instructive to examine the conditions under which the reduction of the charge evolution equation (2.4) and associated boundary condition was possible. The requirement is that  $\rho \ll 2ec_\infty$ .

For the semi-infinite space, (3.5) and (3.11) lead to the requirement

$$Re \left\{ \frac{\sigma_0 \kappa^2}{P} \right\} < \frac{\sigma_0 \kappa^2}{R(\kappa, k, \omega/D)} \equiv \frac{\epsilon E \kappa^2}{\left[ (\kappa^2 + k^2)^2 + \left( \frac{\omega}{D} \right)^2 \right]^{1/4}} \ll 2ec_\infty, \quad (\text{A1})$$

and this is analogous (but not identical) to the criterion reported by Ehrlich & Melcher (1982, below their figure 5) for the  $k = 0$  case. This condition then poses an upper bound on the electric field amplitude in such a semi-infinite space.

Equation (A1) can be reexpressed more clearly by eliminating  $ec_\infty$  in favour of  $\kappa$  through (2.6)

$$f(\kappa, E) \equiv \frac{eE}{k_B T \left[ (\kappa^2 + k^2)^2 + \left( \frac{\omega}{D} \right)^2 \right]^{1/4}} \ll 1. \quad (\text{A2})$$

In retrospect, if we define an ‘applied’ potential  $\phi_a \equiv E/R$ , (A2) is nothing else than the statement

$$\frac{\phi_a}{\phi_T} \ll 1, \quad (\text{A3})$$

where  $\phi_T \equiv k_B T/e \sim 0.0253 \text{ V}$  is the thermal potential. The bounds (A2) and (A3) differ from the standard Debye–Hückel approximation (see (A4)) in that the wavenumber  $\kappa$  in the latter is replaced here by the commensurate wavenumber  $R(\kappa, k, \omega/D) = [(\kappa^2 + k^2)^2 + (\omega/D)^2]^{1/4}$  defined in (3.11). Thus, even for moderate frequencies  $\omega \sim 10^2 \text{ rad s}^{-1}$ , as shown in figure 11(a), the approximation under consideration significantly improves compared with its Debye–Hückel counterpart (figure 11c). This is the case because the

wavenumber  $R(\kappa, k, \omega/D)$  can become arbitrarily large when the frequency  $\omega$  (present because of the time derivative in (2.2)) is moderate to high, even for small Debye lengths.

In figures 11(a) and 11(b), we plot contours of the function  $f(\kappa, E)$  in (A2) for the constant values  $f = 1, 0.1, 0.01$  and  $0.001$  for  $k = 10^5 \text{ m}^{-1}$  and  $D = 10^{-9} \text{ m}^2 \text{ s}^{-1}$  at room temperature. It is thus seen that the range of validity of the approximation increases as the frequency  $\omega$  (or the ratio  $\omega/D$ ) increases.

In the small-Debye-length limit, (A1) becomes  $\sigma_0 \kappa \ll 2c_\infty$ . Eliminating  $c_\infty$  (or taking the large  $\kappa$  limit in (A2)), we obtain the following bound:

$$\frac{eE}{\kappa k_B T} \ll 1. \quad (\text{A4})$$

This is analogous to the Debye–Hückel approximation where  $e\phi \ll k_B T$  (Melcher 1981, p. 10.22) if the characteristic length scale of the system is the Debye length. In figure 11(c), we plot contours of the function  $eE/\kappa k_B T$  at room temperature. Clearly, the range of validity of the approximation leading to the bound (A2) and displayed in figures 11(a) and 11(b) is superior.

In the bounded geometry of a channel of width  $2h$ , (4.2) leads to the requirement

$$Re \left\{ \frac{\sigma_0 \kappa^2 \cos Pz}{P \sin Ph} \right\} \leq \frac{\sigma_0 \kappa^2 \coth(P_2 h)}{R(\kappa, k, \omega/D)} \equiv \frac{\epsilon E \kappa^2 \coth(P_2 h)}{\left[ (\kappa^2 + k^2)^2 + \left( \frac{\omega}{D} \right)^2 \right]^{\frac{1}{4}}} \ll 2ec_\infty, \quad (\text{A5})$$

where  $P_2(\kappa, k, \omega/D) = 1/(\sqrt{2})\sqrt{R^2 + \kappa^2 + k^2}$  was defined in (3.4) and  $R$  in (3.11). Equation (A5) differs from its semi-infinite space counterpart equation (A1) only by the factor  $\coth(P_2 h)$ . For all practical purposes, this factor nearly equals 1 and does not affect the approximation in a significant manner when the frequency  $\omega$  is non-vanishing.

## A.2. Comparison of the Debye–Falkenhagen with the Debye–Hückel approximation

The vast majority of electroosmosis formulations employ the Debye–Hückel approximation which amounts to setting the time derivative in (2.4) equal to zero. This gives a linear relation between  $\rho$  and  $\phi$ , explicitly,  $\rho = -\epsilon \kappa^2 \phi$ . However,  $\rho$  and  $\phi$  in this paper are related through

$$\rho = \epsilon \left( \frac{i\omega}{D} - \kappa^2 \right) \left\{ \phi + \frac{\sigma_0}{\epsilon} \left[ \frac{\frac{i\omega}{D}}{\frac{i\omega}{D} - \kappa^2} \right] \frac{e^{-kz}}{k} e^{i(kx - \omega t)} \right\} \quad (\text{A6})$$

cf. (3.6). It clearly reduces to the form  $\rho = -\epsilon \kappa^2 \phi$  in the limit  $\omega \rightarrow 0$ . Second, in the Debye–Hückel case,  $\phi$  and  $\rho \sim e^{-\kappa z}$  by solving either  $\partial_z^2 \rho = \kappa^2 \rho$  or equivalently,  $\partial_z^2 \phi = \kappa^2 \phi$ . In contrast, in our case,  $\rho \sim e^{-P_2 z} e^{i(P_1 z + kx - \omega t)}$ , where  $P_1$  and  $P_2$  were defined in (3.4). Thus, in this paper, the penetration depth is  $1/P_2$ . The Debye–Hückel penetration depth  $\kappa^{-1}$  has been renormalised by excitation wavenumber  $k$ , frequency  $\omega$  and species diffusion coefficient  $D$ . Plane waves propagate in both the  $x$  and the  $z$  directions, the latter with a composite wavenumber  $P_1$ .

## Appendix B. Effect of the advection terms in the Nernst–Planck equation

### B.1. Validity of dropping the advection terms in the Nernst–Planck equation

In the main body of this paper, the advective term of (2.4) was neglected based on a small-Péclet-number approximation. Here, we justify the validity of this approach.

Choosing characteristic scales appropriate for a long and thin configuration (similar to the lubrication approximation, cf. Davis 2002; Kirkinis & Davis 2015), we introduce new dimensionless variables

$$X = kx, \quad Z = \kappa z, \quad U = \frac{u}{u_0}, \quad V = \frac{v}{u_0 \frac{\kappa}{k}}, \quad \tau = D\kappa^2 t, \quad (\text{B1})$$

where  $u_0$  is the velocity scale defined in (2.12). Equation (2.4) becomes

$$\partial_\tau \rho = \left[ \left( \frac{k}{\kappa} \right)^2 \partial_X^2 + \partial_Z^2 - 1 \right] \rho - Pe \frac{k}{\kappa} (U \partial_X + V \partial_Z) \rho \quad (\text{B2})$$

where

$$Pe = \frac{u_0}{\kappa D}. \quad (\text{B3})$$

This Péclet number scales quadratically with respect to the Debye length. Employing standard parameter values for water  $\epsilon = 7 \times 10^{-10} \text{ F m}^{-1}$ ,  $\eta = 0.001 \text{ kg m}^{-1} \text{ s}$ ,  $\kappa = 10^7 \text{ m}^{-1}$  (Debye length equal to hundreds of nanometres),  $E = 10^5 \text{ V m}^{-1}$  and thus  $u_0 \sim 0.35 \text{ mm s}^{-1}$ , we obtain the estimate

$$Pe \sim 0.035. \quad (\text{B4})$$

When the Debye length is even smaller (say only tens of nanometres or the electric field smaller, say  $E = 10^4 \text{ V m}^{-1}$ ), the Péclet number estimate (B4) is further reduced by two orders of magnitude.

## B.2. Effect of Péclet number on the zero mode

When the Péclet number is small, the fields can be expanded in a regular perturbation series with respect to this small number. In particular, the streamfunction will be of the form

$$\psi = \psi_0(z) + Pe \psi_1(z) e^{i\theta} + Pe^2 \psi_2(z) e^{2i\theta} + \dots + c.c., \quad (\text{B5})$$

where  $\theta = kx - \omega t$ , *c.c.* denotes complex conjugate terms and  $\psi_0$  is the zero-mode streamfunction ( $u(z) = \partial_z \psi_0$ ). Such an expansion has been applied in the past to obtain amplitude equations of singularly perturbed nonlinear partial differential equations such as the Kuramoto–Sivashinsky and the Swift–Hohenberg equations cf. Kirkinis & O'Malley Jr. (2014) and references therein, as well as other linear and nonlinear problems (O'Malley & Kirkinis 2010, 2011). In this appendix, we will retain only the  $O(Pe^0)$  term in expansion (B5) which will provide contributions to the advection term in the Nernst–Planck equation (B2). To be specific, we employ the channel geometry of § 4. Let

$$\rho = R + iJ, \quad \rho^* = R - iJ, \quad \phi = \Phi + i\Omega, \quad \phi^* = \Phi - i\Omega, \quad (\text{B6})$$

for real fields  $R$ ,  $J$ ,  $\Phi$  and  $\Omega$ . The dimensional form of the Poisson–Nernst–Planck–Stokes equations for these fields becomes

$$J_{zz} - K^2 J = -\frac{\omega}{D} R + \frac{k}{D} Ru, \quad R_{zz} - K^2 R = \frac{\omega}{D} J - \frac{k}{D} Ju, \quad (\text{B7})$$

and

$$\Phi_{zz} - k^2 \Phi = -\frac{R}{\epsilon}, \quad \Omega_{zz} - k^2 \Omega = -\frac{J}{\epsilon}, \quad u_z = \frac{\epsilon k}{2\eta} (\Omega \Phi_z - \Phi \Omega_z), \quad (\text{B8})$$

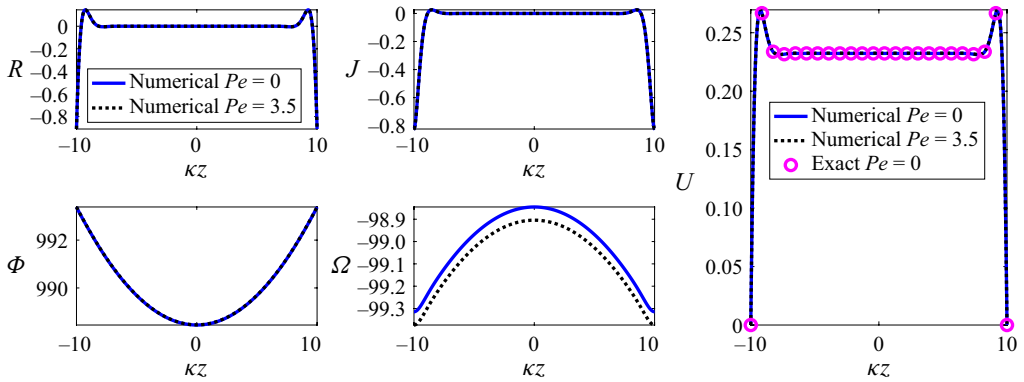


Figure 12. Determination of the effect of the Péclet number on the zero-mode velocity in a channel. Plot of the dimensionless fields  $R$ ,  $J$ ,  $\Phi$ ,  $\Omega$  and  $U$  by solving (B11) and (B12) with boundary conditions (B13). The numerical solution for zero Péclet number (continuous curve) is nearly identical to the numerical solution for an exaggerated value of  $Pe = 3.5$  (dotted curve). The circles denote the exact velocity (4.5) (which was determined for zero Péclet number). Here, we have taken  $\kappa = 10^6 \text{ m}^{-1}$ ,  $D = 10^{-9} \text{ m}^2 \text{ s}^{-1}$ ,  $k = 10^4 \text{ m}^{-1}$ ,  $h = 10^{-5} \text{ m}$  and  $\omega = 10 \times D\kappa^2$ .

where  $K = \sqrt{\kappa^2 + k^2}$ . We also need nine boundary conditions at  $z = \mp h$ ,

$$R_z(\mp h) = \mp \sigma_0 \kappa^2, \quad J_z(\mp h) = 0, \quad \Phi_z(\mp h) = \pm \frac{\sigma_0}{\epsilon}, \quad \Omega_z(\mp h) = 0, \quad u(-h) = 0. \quad (\text{B9})$$

The above equations and boundary conditions are non-dimensionalised by employing (B1) and (B3) and the fields

$$(\hat{R}, \hat{J}) = \frac{(R, J)}{2ec_\infty}, \quad (\hat{\Phi}, \hat{\Omega}) = \frac{(\Phi, \Omega)\kappa}{E}, \quad \hat{U} = \frac{u}{u_0}, \quad H = \kappa h, \quad (\text{B10})$$

where  $E$  is a characteristic scale for the applied electric field ( $E \sim \sigma_0/\epsilon$ ),  $u_0$  is the velocity scale defined in (2.12) and  $h$  is the dimensional width of the channel.

Equations (B7), (B8) and their boundary conditions (B9) become in dimensionless units (dropping the hats)

$$R_{ZZ} - \left(\frac{K}{\kappa}\right)^2 R = \frac{\omega}{D\kappa^2} J - \frac{k}{\kappa} Pe JU, \quad J_{ZZ} - \left(\frac{K}{\kappa}\right)^2 J = -\frac{\omega}{D\kappa^2} R + \frac{k}{\kappa} Pe RU, \quad (\text{B11})$$

$$\Phi_{ZZ} - \left(\frac{k}{\kappa}\right)^2 \Phi = -\frac{\phi_T}{\phi_A} R, \quad \Omega_{ZZ} - \left(\frac{k}{\kappa}\right)^2 \Omega = -\frac{\phi_T}{\phi_A} J, \quad U_Z = \frac{k}{\kappa} [\Omega \Phi_Z - \Phi \Omega_Z] \quad (\text{B12})$$

$$R_Z(\mp H) = \pm \frac{\phi_A}{\phi_T}, \quad J_Z(\mp H) = 0, \quad \Phi_Z(\mp H) = \mp 1, \quad \Omega_Z(\mp H) = 0, \quad U(-H) = 0, \quad (\text{B13})$$

where

$$\phi_A = \frac{E}{\kappa}, \quad \phi_T = \frac{k_B T}{e} \quad (\text{B14})$$

are the applied and thermal electric potentials, respectively, and the Péclet number  $Pe$  was defined in (B3).



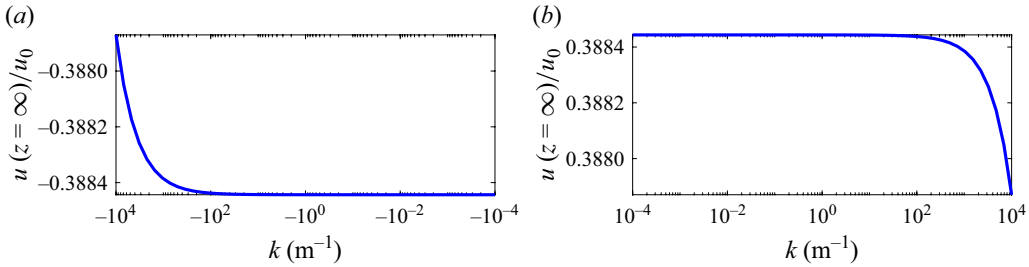


Figure 13. (a) Negative and (b) positive zero velocity branch (3.10) as a function of  $k$ . The velocity is discontinuous at  $k = 0$  which is (C2), cf. Ehrlich & Melcher (1982, (34)). Here, we have taken  $\kappa = 10^7 \text{ m}^{-1}$  and  $D = 10^{-9} \text{ m}^2 \text{ s}^{-1}$ .

Equations (B11) and (B12) with boundary conditions (B13) form a nonlinear first-order system of nine equations that is solved with a boundary value solver. In figure 12, we display the numerical solution of the system for zero Péclet number (continuous curve) and for an exaggerated value of  $Pe = 3.5$  (dotted curve). The circles denote the exact velocity (4.5) (which was determined for zero Péclet number). The two numerical solutions of differing Péclet numbers agree very well. The conclusion is that the advection terms in the Nernst–Planck equation (B2) do not significantly alter the zero mode (when higher order harmonics can be safely neglected).

### Appendix C. The Ehrlich & Melcher (1982) ‘slip’ velocity

Figures 13(a) and 13(b) display the plus/minus branch of the velocity (3.10), corresponding to positive/negative  $k$ , respectively. From figure 13, it is apparent that the velocity at  $k = 0$  displays a discontinuity. This particular case has appeared before in the literature (Ehrlich & Melcher 1982). Introducing the time scale (in the notation of Ehrlich & Melcher (1982)),

$$t_e \equiv \frac{\epsilon k_B T}{2c_\infty e^2 D} = \frac{1}{D\kappa^2}, \quad (\text{C1})$$

where  $\kappa$  was defined in (2.6), and setting  $k = 0$  leads the amplitude and phase in (3.11) to obtain the form  $R = \kappa[1 + (\omega t_e)^2]^{1/4}$  and  $\Theta = -(1/2) \arctan(\omega t_e) + (\pi/2)$ . Substituting into (3.10) and setting  $k = 0$ , we obtain

$$u(\infty) = \frac{\omega t_e}{(\omega^2 t_e^2 + 1)^{5/4}} \cos\left(\frac{\arctan(\omega t_e)}{2}\right), \quad (\text{C2})$$

which is equation (34) of Ehrlich & Melcher (1982) and  $t_e$  was defined in (C1). In figure 3(a) (continuous curve), we display (C2), which recovers (in logarithmic axes) figure 3 of Ehrlich & Melcher (1982).

### Appendix D. Relation of solution ansatz $\phi(z)e^{i(kx-\omega t)}$ to other literature

The form of the electric potential we have assumed to be true  $\phi(z)e^{i(kx-\omega t)}$  in a space that is infinitely long in the  $x$ -direction is of the same form employed to describe gravity waves in potential flow, that is, when the velocity of the liquid can be written as the gradient of a scalar function  $\phi$ , which satisfies Laplace’s equation with (nearly) Neumann (but homogeneous) boundary conditions (Landau & Lifshitz 1987, § 12). For instance, the resulting velocity field of a liquid of depth  $h$  obtains the form

$$\mathbf{v}(x, z, t) = \frac{A\omega}{\sinh(kh)} (-\cosh(k(z+h)) \sin(kx - \omega t), \sinh(k(z+h)) \cos(kx - \omega t)) \quad (\text{D1})$$

which essentially equals the electric field obtained from the channel case from (4.3) in the absence of an electrolyte.

## Appendix E. Channel closed-form zero-mode velocity

Consider the function

$$\begin{aligned} \mathfrak{F}(z) = & \frac{A^*B}{2} \left( -\frac{(k+iP) \cosh((k-iP)z)}{k-iP} - \frac{(k-iP) \cosh((k+iP)z)}{k+iP} \right) \\ & + \frac{B^*A}{2} \left( \frac{(k-iP^*) \cosh((k+iP^*)z)}{k+iP^*} + \frac{(k+iP^*) \cosh((k-iP^*)z)}{k-iP^*} \right) \\ & + \frac{|B|^2}{2} \left( \frac{(P+P^*) \cosh((P-P^*)z)}{P-P^*} + \frac{(P-P^*) \cosh((P+P^*)z)}{P+P^*} \right), \quad (\text{E1}) \end{aligned}$$

where

$$A = \frac{\sigma_0 \left(1 + \frac{\kappa^2}{P^2 + k^2}\right)}{\epsilon k \sinh(kh)}, \quad B = \frac{\sigma_0 \kappa^2}{\epsilon (P^2 + k^2) P \sin(Ph)}. \quad (\text{E2})$$

Then,

$$u(z) = \frac{i\epsilon k}{4\eta} [\mathfrak{F}(z) - \mathfrak{F}(h)] \quad (\text{E3})$$

is the closed-form expression for the zero-mode velocity (4.5) of the rectangular channel of § 4.

Defining the function

$$\begin{aligned} \mathfrak{G}(z) = & \frac{A^*B}{2} \left( -\frac{(k+iP) \sinh((k-iP)z)}{(k-iP)^2} - \frac{(k-iP) \sinh((k+iP)z)}{(k+iP)^2} \right) \\ & + \frac{B^*A}{2} \left( \frac{(k-iP^*) \sinh((k+iP^*)z)}{(k+iP^*)^2} + \frac{(k+iP^*) \sinh((k-iP^*)z)}{(k-iP^*)^2} \right) \\ & + \frac{|B|^2}{2} \left( \frac{(P+P^*) \sinh((P-P^*)z)}{(P-P^*)^2} + \frac{(P-P^*) \sinh((P+P^*)z)}{(P+P^*)^2} \right), \quad (\text{E4}) \end{aligned}$$

which is the indefinite integral of  $\mathfrak{F}$ , we can express in succinct form the average value of the zero mode (4.6),

$$\langle u \rangle = \frac{i\epsilon k}{4\eta h} [\mathfrak{G}(h) - h\mathfrak{F}(h)], \quad (\text{E5})$$

which is displayed in figures 5(a) and 6(a) with circle and triangular markers.

## Appendix F. Dirichlet problem: travelling wave electric potentials at a wall

In the main body of this paper, we employed Neumann boundary conditions that fix the normal electric field on a charged wall. In the following discussion, we will replace them with Dirichlet boundary conditions, that is, a fixed electric potential on the wall.

### F.1. Semi-infinite space

We consider the configuration displayed in [figure 1](#), where now the travelling wave surface charges must be replaced by travelling wall electric potentials on the wall  $z = 0$  bounding an 1 : 1 electrolyte lying in the semi-infinite space  $z > 0$ . The boundary conditions satisfied by the charge  $\rho$  and potential  $\phi$  are

$$\phi(x, z = 0) = \phi_0 e^{i(kx - \omega t)}, \quad \partial_z \rho(x, z = 0, t) = -\epsilon \kappa^2 \partial_z \phi(x, z = 0, t), \quad (\text{F1})$$

the latter being the zero current condition  $\mathbf{J} \cdot \hat{\mathbf{z}} = -D[\nabla \rho + (e/k_B T) s \nabla \phi] \cdot \hat{\mathbf{z}} = 0$  at the same wall, lead to the requirement that  $\partial_z \rho = -\epsilon \kappa^2 \partial_z \phi$ . These can be satisfied only after both fields are determined up to arbitrary constants  $\rho(z) = A e^{iPz}$ ,  $\phi(z) = B e^{-kz} + (A/\epsilon(P^2 + k^2)) e^{iPz}$ . The charge distribution reads

$$\rho(x, z, t) = \frac{\epsilon \kappa^2 k \phi_0 (P^2 + k^2)}{i P (P^2 + \kappa^2 + k^2) + k \kappa^2} e^{i(Pz + kx - \omega t)}, \quad (\text{F2})$$

where  $P$  is again expressed by (3.3). In the absence of potential modulation ( $k = 0$ ), the charge is zero everywhere. For non-zero  $k$ , the penetration depth is again determined by the inverse of the imaginary part of  $P$  (taken to be positive).

Similarly, assuming  $\phi = \phi(z) e^{i(kx - \omega t)}$ , (2.2) reduces to  $\phi_{zz} - k^2 \phi = -(\kappa^2 k \phi_0 (P^2 + k^2)) / (i P (P^2 + \kappa^2 + k^2) + k \kappa^2) e^{iPz}$ , subject to the boundary condition (F1) and  $\phi = 0$  at infinity. Thus, the potential distribution reads

$$\phi(x, z, t) = \phi_0 \left( 1 - \frac{k \kappa^2}{i P (P^2 + \kappa^2 + k^2) + k \kappa^2} \right) e^{-kz} e^{i(kx - \omega t)} + \frac{1}{\epsilon (P^2 + k^2)} \rho, \quad (\text{F3})$$

with  $\rho$  given by (F2) and we assumed that  $k > 0$ .

### F.2. Channel case

The boundary conditions satisfied by the charge  $\rho$  and potential  $\phi$  are

$$\phi(x, z = \pm h) = \phi_0 e^{i(kx - \omega t)}, \quad \partial_z \rho(x, z = \pm h, t) = -\epsilon \kappa^2 \partial_z \phi(x, z = \pm h, t), \quad (\text{F4})$$

the charge distribution reads

$$\rho(x, z, t) = \frac{\phi_0 \epsilon (P^2 + k^2) \sinh(kh) \kappa^2 k \cos(Pz) e^{i(kx - \omega t)}}{P \sin(Ph) (P^2 + k^2 + \kappa^2) \cosh(kh) + \sinh(kh) \kappa^2 k \cos(Ph)}, \quad (\text{F5})$$

where  $P$  is the complex wavenumber displayed in (3.3). Note that the denominator of expression (F5) is composed of hyperbolic functions of large argument (since  $P$  is complex) so, close to the centre of the channel ( $z = 0$ ), the charge is effectively zero, cf. Ajdari (1995, (4)) for the corresponding case of a steady periodic wall charge distribution.

Similarly, assuming  $\phi = \phi(z) e^{i(kx - \omega t)}$  and subject to the boundary condition (F4), the electric potential distribution reads

$$\begin{aligned} \phi(x, z, t) = & \frac{\sin(Ph) P (P^2 + k^2 + \kappa^2) \phi_0 \cosh(kz) e^{i(kx - \omega t)}}{P \sin(Ph) (P^2 + k^2 + \kappa^2) \cosh(kh) + \sinh(kh) \kappa^2 k \cos(Ph)} \\ & + \frac{1}{\epsilon (P^2 + k^2)} \rho, \end{aligned} \quad (\text{F6})$$

with  $\rho$  given by (F5).

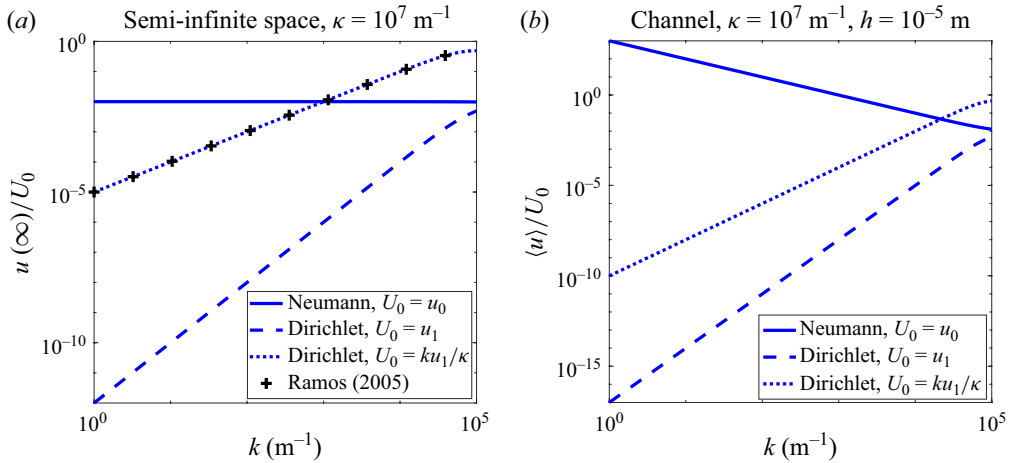


Figure 14. (a) Semi-infinite space zero-mode velocity (3.10) versus the wall excitation wavenumber  $k$ , obtained with Neumann or Dirichlet boundary conditions (employing the potentials (4.3) and (F6), respectively) and scaled by either  $u_0$  or  $ku_1/\kappa$  (cf. (2.12)). Each line, from top to bottom, has slope 0, 1 and 2, respectively, determining the velocity  $k$ -dependence as  $k^0$ ,  $k^1$  and  $k^2$ , respectively. The plus sign markers denote the theoretical velocity expression of Ramos *et al.* (2005, (10)),  $\Omega/(1 + \Omega^2)$ , where  $\Omega = \omega/D\kappa$ , which (nearly) coincides with the Dirichlet velocity when the scaling employed is  $ku_1/\kappa$ . The Dirichlet behaviour is reminiscent of that observed in figure 6(a) of Cahill *et al.* (2004). (b) Average of the channel width zero-mode velocity (4.7) versus the wall excitation wavenumber  $k$ , obtained with Neumann or Dirichlet boundary conditions and scalings as above. Each line, from top to bottom, has slope  $-1$ , 2 and 3, respectively, determining the velocity  $k$ -dependence as  $k^{-1}$ ,  $k^2$  and  $k^3$ , respectively. The Neuman curve  $k$  behaviour is reminiscent of figure 6(f) of Liu *et al.* (2018), where the slip velocity increases linearly with the excitation wavelength. In both panels,  $\omega = 10^3 \text{ Hz}$ .

## Appendix G. The $k$ dependence of the velocities

The preceding discussion, although informative, does not provide an understanding of the magnitude of the effects, which we thus analyse in the present section.

Figure 14(a) displays the  $k$ -dependence of the  $u(\infty)$  zero-mode velocity (3.10) versus the wall excitation wavenumber  $k$ , obtained with Neumann and with Dirichlet boundary conditions (employing the potentials (4.3) and (F6), respectively) and scaled by either  $u_0$  or  $ku_1/\kappa$  (cf. (2.12)). Each line, from top to bottom, has slope 0, 1 and 2, respectively, determining the velocity  $k$ -dependence as  $k^0$ ,  $k^1$  and  $k^2$ , respectively. It is thus seen that the Neumann curve is nearly constant and essentially impervious to  $k$  (as was also concluded in figure 3a). The theoretical expression for the velocity determined by (10) of Ramos *et al.* (2005), cf. (3.14) below, is nearly identical to the Dirichlet velocity when the scaling employed is  $ku_1/\kappa$  in (2.12).

We repeat the above analysis but for the case of the channel in figure 14(b) which displays the  $k$ -dependence of the average of the channel width zero-mode velocity (4.7) obtained with Neumann and with Dirichlet boundary conditions (employing the potentials (4.3) and (F6), respectively) and scaled by either  $u_0$  or  $ku_1/\kappa$  (cf. (2.12)). Each line, from top to bottom, has slope  $-1$ , 2 and 3, respectively, determining the velocity  $k$ -dependence as  $k^{-1}$ ,  $k^2$  and  $k^3$ , respectively. The Neuman curve  $k$  behaviour is reminiscent of figure 6f of Liu *et al.* (2018), where the slip velocity increases linearly with the excitation wavelength. The  $k$  scaling behaviour of the velocities of interest in this paper is summarised in table 2.

The difference in  $k$ -dependence of the field amplitude  $\phi(z)$  for Neumann and Dirichlet boundary conditions, as is displayed in table 2, can be explained by resorting to a general

	Neumann	Dirichlet
Semi-infinite space	$u(\infty) \sim \text{const.}$	$u(\infty) \sim k^2$
Channel/Capillary	$\langle u \rangle \sim k^{-1}$	$\langle u \rangle \sim k^3$
Channel/Capillary	$\langle u \rangle \sim O(h^0)$	$\langle u \rangle \sim O(h^2)$

Table 2. Summary of scaling behaviour of the (zero mode) velocity. Compare with figure 14. Angle brackets  $\langle \cdot \rangle$  denote averaging over the width of the channel. We also include the limits of the expressions as  $h \rightarrow 0$  from (4.13).

principle known as Stokes' rule (Zauderer 1989, p. 258): if  $\phi$  satisfies Laplace's equation with Neumann boundary conditions  $\partial_z \phi = g(x)$ , then the function  $\chi(z) \equiv \partial_z \phi$  satisfies Laplace's equation with Dirichlet boundary conditions of the form  $\chi = g(x)$  on the same boundary. Thus, if  $\chi \sim O(k^\alpha)$ , then its integral with respect to  $z$  is of  $O(k^{\alpha-1})$ , which is the behaviour met here when solving the Poisson equation with Neumann and Dirichlet boundary conditions (to obtain this explicit behaviour, we tacitly assumed that  $g(x) \sim e^{ikx}$ , and thus both  $\phi$  and  $\chi$  vary harmonically in the  $x$  direction).

## Appendix H. Simplification of the nonlinear electric force and torque in the momentum equation

### H.1. Simplification of the nonlinear torque in (2.8)

In this appendix, we reduce the fourth-order vorticity equation (2.8) to the first-order (3.7). Let

$$2\rho = \rho(z)e^{i\theta} + \rho^*(z)e^{-i\theta}, \quad 2\phi = \phi(z)e^{i\theta} + \phi^*(z)e^{-i\theta}, \quad 2\rho_x = ik \left( \rho(z)e^{i\theta} - \rho^*(z)e^{-i\theta} \right), \quad (\text{H1})$$

etc., with a slight abuse of notation, where  $\theta = kx - \omega t$ . Thus, after averaging over the period of oscillation, the nonlinear term in  $\eta \partial_z^3 u(z) = \rho_z \phi_x - \rho_x \phi_z$  becomes

$$4(\rho_z \phi_x - \rho_x \phi_z) = ik (\phi \rho_z^* - \phi^* \rho_z + \phi_z \rho^* - \rho \phi_z^*) \quad (\text{H2})$$

$$= i\epsilon k (\phi_{zzz} \phi^* - \phi \phi_{zzz}^* + \phi_z^* \phi_{zz} - \phi_z \phi_{zz}^*) \quad (\text{H3})$$

$$= i\epsilon k (\phi^* \phi_z - \phi \phi_z^*)_{zz}, \quad (\text{H4})$$

where we replaced  $\rho$  by  $\epsilon(k^2 \phi - \phi_{zz})$ . In summary,  $4\eta \partial_z^3 u(z) = i\epsilon k (\phi^* \phi_z - \phi \phi_z^*)_{zz}$  or

$$u'(z) = \frac{i\epsilon k}{4\eta} (\phi^* \phi_z - \phi \phi_z^*) + Az + B. \quad (\text{H5})$$

The two constants of integration drop out. In the semi-infinite case, where the velocity at the wall is zero and at  $z = \infty$  finite, the expression on the right-hand side of (H5) vanishes (it is composed of decaying exponentials), so  $A \equiv 0$ , while performing an extra integration leads to the vanishing of  $B$  since the velocity can only be finite at  $z = \infty$ . Thus,  $u(z) = \mathcal{G}(z) - \mathcal{G}(0)$ , where  $\mathcal{G}(z)$  is the integral of the first term on the right-hand side of (H5). Thus,  $u(\infty) = -\mathcal{G}(0)$ .

Likewise, in the channel case,  $A$  is the pressure gradient in the  $x$ -direction of the momentum equation (which is zero) and  $B$  vanishes based on the antisymmetry of the first term on the right-hand side of (H5) with respect to  $z$  (and since  $\partial_z u|_{z=0} = 0$ ).

## H.2. Equivalence of (H5) to the time-dependent Stokes equations

Equation (H5) was derived by integrating twice the vorticity equation for the zero mode. Below, we show how (H5) can directly be derived from the Navier–Stokes equations.

There is no pressure gradient in the  $x$ -direction,  $\mathcal{P}_x = 0$ , otherwise it would give rise to a commensurate pressure-driven flow. Thus, the  $x$ -component of the Navier–Stokes equation is simply

$$\eta u_{zz} = \rho \phi_x, \quad (\text{H6})$$

where the right-hand side implies that the observables are real. With the same notation as in (H1) and replacing  $\rho$  by  $\epsilon(k^2\phi - \phi_{zz})$ , we obtain

$$4\rho\phi_x = i\epsilon k^3(\phi^2 - (\phi^*)^2) - i\epsilon k(\phi\phi_{zz} - \phi^*\phi_{zz}^* + \phi\phi_{zz}^* - \phi^*\phi_{zz}^{*}) = i\epsilon k(\phi^*\phi_z - \phi\phi_z^*)_z \quad (\text{H7})$$

and in the last step, we integrated over the period of oscillation. Thus, substituting into (H6) leads to (H5).

It is also easy to show that the  $z$ -component of the Navier–Stokes equations leads to the pressure expression

$$4\mathcal{P} = \epsilon(k^2|\phi|^2 - |\phi_z|^2) \quad (\text{H8})$$

after averaging over the period of oscillation. Thus, the hydrodynamic pressure  $\mathcal{P}$  only depends on the vertical coordinate  $z$ , causing  $\mathcal{P}_x$  to vanish, as required by (H6).

## REFERENCES

- AJDARI, A. 1995 Electro-osmosis on inhomogeneously charged surfaces. *Phys. Rev. Lett.* **75** (4), 755–758.
- AJDARI, A. 2000 Pumping liquids using asymmetric electrode arrays. *Phys. Rev. E* **61** (1), R45–R48.
- BAZANT, M.Z., THORNTON, K. & AJDARI, A. 2004 Diffuse-charge dynamics in electrochemical systems. *Phys. Rev. E* **70** (2), 021506.
- BLUMAN, G.W. & KUMEI, S. 1989 *Symmetries and differential equations*. Springer.
- CAHILL, B.P., HEYDERMAN, L.J., GOBRECHT, J. & STEMMER, A. 2004 Electro-osmotic streaming on application of traveling-wave electric fields. *Phys. Rev. E* **70** (3), 036305.
- CLARKE, B.M.N. & STILES, P.J. 2015 Finite electric boundary-layer solutions of a generalized Poisson–Boltzmann equation. *Proc. R. Soc. Lond. A: Math. Phys. Engng Sci.* **471**(2178), 20150024.
- CONSTANTIN, P., IGNATOVA, M. & LEE, F.-N. 2021 Nernst–Planck–Navier–Stokes systems far from equilibrium. *Arch. Ration. Mech. Anal.* **240** (2), 1147–1168.
- CONSTANTIN, P., IGNATOVA, M. & LEE, F.-N. 2022 Existence and stability of nonequilibrium steady states of Nernst–Planck–Navier–Stokes systems. *Physica D: Nonlinear Phenom.* **442**, 133536.
- DAVIS, S.H. 2002 Interfacial fluid dynamics. In *Perspectives in Fluid Dynamics: A Collective Introduction to Current Research* (ed. G.K. BATCHELOR, H.K. MOFFATT & M.G. WORSTER), pp. 1–51. Cambridge University Press.
- EHRlich, R.M. & MELCHER, J.R. 1982 Bipolar model for traveling-wave induced nonequilibrium double-layer streaming in insulating liquids. *Phys. Fluids* **25** (10), 1785–1793.
- GARCÍA-SÁNCHEZ, P., RAMOS, A., GREEN, N.G. & MORGAN, H. 2006 Experiments on AC electrokinetic pumping of liquids using arrays of microelectrodes. *IEEE Trans. Dielec. Elec. Insul.* **13** (3), 670–677.
- GOLDSTONE, J. 1961 Field theories with superconductor solutions. *Il Nuovo Cimento* **19** (1), 154–164.
- GONZÁLEZ, A., RAMOS, A. & CASTELLANOS, A. 2008 Pumping of electrolytes using travelling-wave electro-osmosis: a weakly nonlinear analysis. *Microfluid. Nanofluid.* **5** (4), 507–515.
- GONZÁLEZ, A., RAMOS, A., GREEN, N.G., CASTELLANOS, A. & MORGAN, H. 2000 Fluid flow induced by nonuniform ac electric fields in electrolytes on microelectrodes. II. A linear double-layer analysis. *Phys. Rev. E* **61** (4), 4019–4028.
- GREEN, N.G., RAMOS, A., GONZÁLEZ, A., MORGAN, H. & CASTELLANOS, A. 2000 Fluid flow induced by nonuniform ac electric fields in electrolytes on microelectrodes. I. Experimental measurements. *Phys. Rev. E* **61** (4), 4011–4018.



- VAN DER HEYDEN, F.H.J., BONTHUIS, D.J., STEIN, D., MEYER, C. & DEKKER, C. 2006 Electrokinetic energy conversion efficiency in nanofluidic channels. *Nano Lett.* **6** (10), 2232–2237.
- VAN DER HEYDEN, F.H.J., BONTHUIS, D.J., STEIN, D., MEYER, C. & DEKKER, C. 2007 Power generation by pressure-driven transport of ions in nanofluidic channels. *Nano Lett.* **7** (4), 1022–1025.
- KAMSMA, T.M., BOON, W.Q., TER RELE, T., SPITONI, C. & VAN ROIJ, R. 2023a Iontronic neuromorphic signaling with conical microfluidic memristors. *Phys. Rev. Lett.* **130** (26), 268401.
- KAMSMA, T.M., BOON, W.Q., SPITONI, C. & VAN ROIJ, R. 2023b Unveiling the capabilities of bipolar conical channels in neuromorphic iontronics. *Faraday Discuss.* **246**, 125–140.
- KIRKINIS, E. & DAVIS, S.H. 2015 Stabilization mechanisms in the evolution of thin liquid-films. *Proc. R. Soc. Lond. A* **471** (2184), 20150651.
- KIRKINIS, E. & O'MALLEY, JR.R.E. 2014 Amplitude modulation for the Swift–Hohenberg and Kuramoto–Sivashinski equations. *J. Math. Phys.* **55** (12), 123510.
- LANDAU, L.D. & LIFSHITZ, E.M. 1987 Fluid mechanics. In *Course of Theoretical Physics*, vol. **6**, Pergamon Press Ltd..
- LIU, W., REN, Y., TAO, Y., LI, Y. & WU, Q. 2018 On traveling-wave field-effect flow control for simultaneous induced-charge electroosmotic pumping and mixing in microfluidics: physical perspectives and theoretical analysis. *J. Micromech. Microengng* **28** (5), 055004.
- LUKE, Y.L. 1962 *Integrals of Bessel Functions*. McGraw-Hill Book Co., Inc.
- MALOMED, B.A. 1992 Patterns produced by a short-wave instability in the presence of a zero mode. *Phys. Rev. A* **45** (2), 1009–1017.
- MELCHER, J.R. 1981 *Continuum Electromechanics*. MIT press.
- MORSE, P.M. & FESHBACH, H. 1953 *Methods of Theoretical Physics*. McGraw Hill Book Company Inc.
- MORTENSEN, N.A., OLESEN, L.H., BELMON, L. & BRUUS, H. 2005 Electrohydrodynamics of binary electrolytes driven by modulated surface potentials. *Phys. Rev. E* **71** (5), 056306.
- NEGELE, J.W. & ORLAND, H. 1988 Quantum many-particle systems. *Frontier Phys.* **68**.
- O'MALLEY, JR., R.E. & KIRKINIS, E. 2010 A combined renormalization group-multiple scale method for singularly perturbed problems. *Stud. Appl. Maths* **124** (4), 383–410.
- O'MALLEY, JR., R.E. & KIRKINIS, E. 2011 Two-timing and matched asymptotic expansions for singular perturbation problems. *Eur. J. Appl. Math.* **22** (6), 613–629.
- PANTON, R.L. 1996 *Incompressible Flow*. John Wiley & Sons Inc.
- PARATORE, F., BACHEVA, V., BERCOVICI, M. & KAIGALA, G.V. 2022 Reconfigurable microfluidics. *Nat. Rev. Chem.* **6** (1), 70–80.
- PROBSTEIN, R.F. 1994 *Physicochemical Hydrodynamics: An Introduction*. John Wiley & Sons.
- RAMOS, A., MORGAN, H., GREEN, N.G., GONZÁLEZ, A. & CASTELLANOS, A. 2005 Pumping of liquids with traveling-wave electroosmosis. *J. Appl. Phys.* **97** (8), 084906.
- YEH, H.-C., YANG, R.-J. & LUO, W.-J. 2011 Analysis of traveling-wave electro-osmotic pumping with double-sided electrode arrays. *Phys. Rev. E* **83** (5), 056326.
- YEN, P.-W., LIN, S.-C., HUANG, Y.-C., HUANG, Y.-J., TUNG, Y.-C., LU, S.-S. & LIN, C.-T. 2019 A low-power CMOS microfluidic pump based on travelling-wave electroosmosis for diluted serum pumping. *Sci. Rep.* **9** (1), 14794.
- ZAUDERER, E. 1989 *Partial Differential Equations of Applied Mathematics*. 2nd edn. John Wiley & Sons Inc., a Wiley-Interscience Publication.